symmetry

MDPI

Article

Coordinated Transient Voltage Support Considering Induction Motor Dynamics in PV-Integrated Distribution Networks Under Symmetrical Faults

Tao Zhou [1], Wenxiang Xu [1,*], Yichen Zhou [2], Yi Wang [3] and Cheng Wang [1]

[1] School of Automation, Nanjing University of Science and Technology, Nanjing 210094, China; zhoutaonjust@njust.edu.cn (T.Z.); chw714@njust.edu.cn (C.W.)
[2] Department of Electrical Engineering, North China Electric Power University, Baoding 071003, China; zhou.yi.chen.1990@163.com
[3] School of Electrical and Information Engineering, Zhengzhou University, Zhengzhou 450001, China; yiwang@zzu.edu.cn
* Correspondence: xwx11w@163.com; Tel.: +86-19153336275

Abstract

During symmetrical faults in photovoltaic (PV)-integrated distribution networks, induction motor (IM) deceleration elevates reactive-power demand and delays post-fault voltage recovery, whereas conventional voltage-driven support can withdraw prematurely upon initial voltage rebound. To resolve this mismatch, this paper proposes a coordinated transient voltage support (CTVS) strategy that explicitly incorporates IM electromechanical dynamics. A coupled differential-algebraic equation (DAE) model integrating third-order IM dynamics, distributed PV (DPV) DC-link dynamics, and network power balance is formulated, from which a trajectory-local closed-loop Q–V sensitivity is derived to characterize location-dependent support effectiveness. The CTVS controller coordinates critical-bus voltage magnitude, voltage-decrease rate, and rotor slip through fixed spatial participation coefficients under local converter current limits and DC-link voltage feedback. Case studies on a modified IEEE 33-bus feeder under Bus-32 three-phase faults demonstrate that, for the representative 140 ms fault, CTVS suppresses post-fault secondary voltage depression and reduces the sustained recovery delay to 23.85 ms, compared with 342.30 ms for local low-voltage ride-through and 390.85 ms for adaptive Q–V droop control. Matched ablations identify slip-conditioned support persistence as the principal contributor to sustained voltage recovery, whereas the fixed spatial coefficients provide a local allocation advantage under unsaturated conditions rather than a separate large-disturbance recovery benefit under the tested conditions.

Keywords: distributed photovoltaics; induction motor; transient voltage support; symmetrical short-circuit fault

Academic Editor: Yang Yu

Received: 22 September 2026
Revised: 27 October 2026
Accepted: 2 November 2026
Published: 5 November 2026

Copyright: © 2026 by the authors. Licensee MDPI, Basel, Switzerland. This article is an open access article distributed under the terms and conditions of the Creative Commons Attribution (CC BY) license.

1. Introduction

The rapid deployment of distributed photovoltaic (DPV) generation is transforming distribution feeders into active networks that provide voltage regulation and dynamic support. Unlike conventional synchronous generation, DPV units are interfaced through power-electronic converters with limited overcurrent capability and little inherent physi-

cal inertia, changing the mechanisms and time scales of power-system stability [1,2]. Understanding transient voltage behavior therefore requires consideration of the interaction between converter control and dynamic loads during faults.

During symmetrical short-circuit faults, voltage sags activate low-voltage ride-through (LVRT) reactive-current support, whose effectiveness is constrained by converter current limits and DC-link energy accumulation [3–5]. Meanwhile, induction motor (IM) loads can decelerate as electromagnetic torque falls below load torque. The resulting increase in slip and reactive-power demand can deepen voltage depression and delay post-fault recovery [6–8]. Although fast converter support can mitigate fault-induced delayed voltage recovery (FIDVR) [9–11], its effectiveness also depends on the electrical distance between DPV sites and the critical motor bus. Effective transient support must therefore account for converter capability, motor recovery, and spatial feeder coupling.

Existing studies have addressed these issues from several perspectives. Local and two-layer Volt/Var control, coordinated active-power curtailment and tap changing, and storage scheduling regulate voltages under high PV penetration [12–16]. Sensitivity-based optimization, robust control, and model predictive control further address spatial coupling and operating uncertainty [17–20], primarily for steady-state or quasi-steady-state regulation. Dynamic load studies characterize IM responses during voltage sags [6–8], while dynamic PV control, smart-inverter support, and PV-STATCOM compensation address short-term voltage recovery [9–11]. Recent work also considers load dynamics and converter siting in grid-support optimization [21], and adapts reactive-voltage regulation to available converter capability [22]. However, voltage-driven support can decrease after voltage rebounds while the motor is still re-accelerating. This mismatch motivates explicit motor-state feedback and an assessment of its contribution relative to spatial allocation under common converter constraints.

To address this issue, this paper proposes a coordinated transient voltage support (CTVS) method incorporating IM dynamics. A differential-algebraic model couples third-order IM electromechanical dynamics, DPV DC-link dynamics, and network power balance. A trajectory-local closed-loop Q–V sensitivity characterizes location-dependent support effectiveness. The controller combines critical-bus voltage magnitude, voltage-decrease rate, and motor slip through fixed site participation coefficients, with local current limits and DC-link voltage feedback. Case studies on a modified IEEE 33-bus feeder compare CTVS with local LVRT and adaptive Q–V droop control under matched conditions. Controller ablations and spatial-response tests distinguish the contribution of slip-conditioned support persistence from spatial allocation, while DC-energy audits and motor-parameter variations clarify the associated trade-offs and operating scope.

Coordination denotes shared critical-bus voltage–slip feedback and multi-site execution under common converter constraints; the spatial coefficients remain fixed. Performance is evaluated for the modified feeder and Bus-32 three-phase faults in Section 5.

2. Dynamic Modeling of DPV–IM Integrated Distribution Networks

2.1. Dynamic Modeling of DPV

The DPV model includes AC power exchange, LVRT support, current limits, and DC-link energy. For unit i rated at S_i, amplitude-invariant dq variables give:

$$\begin{aligned} P_i &= \frac{3}{2}\left(u_{d,i}i_{d,i} + u_{q,i}i_{q,i}\right) \\ Q_i &= \frac{3}{2}\left(u_{q,i}i_{d,i} - u_{d,i}i_{q,i}\right) \end{aligned} \tag{1}$$

where $u_{d,i}$, $u_{q,i}$, $i_{d,i}$, and $i_{q,i}$ are physical peak PCC-voltage and converter-current components, with current positive into the network. When the d-axis aligns with voltage, positive

reactive injection requires negative signed *q*-axis current; the nonnegative support current in Section 4 uses its negative after per-unit conversion. The rated rms current base is $S_i/(\sqrt{3}V_{\mathrm{LL},i})$, with rated line-to-line voltage $V_{LL,i}$ and peak-base multiplier $\sqrt{2}$.

Under normal operation, the active-power reference follows the maximum power point tracking (MPPT) command. During a voltage sag, the LVRT controller increases the reactive-current reference to support the terminal voltage:

$$\begin{aligned} i_{q,i}^{*,\mathrm{pu}} &= -F_i(V_i) \\ F_i(V_i) &\geq 0 \end{aligned} \tag{2}$$

where V_i is the per-unit PCC voltage magnitude and F_i denotes the nonnegative LVRT reactive-support characteristic. The corresponding positive support-current magnitude is used in the control formulation of Section 4.

The converter-current references must satisfy their device/thermal limit:

$$\left(i_{d,i}^{*,\mathrm{pu}}\right)^2 + \left(i_{q,i}^{*,\mathrm{pu}}\right)^2 \leq I_{\mathrm{max},i}^2 \tag{3}$$

where $I_{\mathrm{max},i}$ uses the site-rated current base; reactive priority leaves the residual capability for active transfer.

Using consistent three-phase power and current bases, the capability constraint at per-unit terminal voltage V_i becomes:

$$\left(\frac{P_i}{S_i}\right)^2 + \left(\frac{Q_i}{S_i}\right)^2 \leq \left(V_i I_{\mathrm{max},i}\right)^2 \tag{4}$$

Reactive support can curtail AC active transfer and charge the DC capacitor through the power imbalance:

$$C_{\mathrm{dc},i} U_{\mathrm{dc},i} \frac{dU_{\mathrm{dc},i}}{dt} = P_{\mathrm{dc},i} - P_{\mathrm{ac},i} \tag{5}$$

Here $C_{dc,i}$ and $U_{dc,i}$ are capacitance and DC voltage, while $P_{dc,i}$ and $P_{ac,i}$ are DC input and modeled AC output powers. With losses neglected, positive imbalance charges the capacitor. The simulation uses an averaged P/Q interface, so $P_{ac,i}$ is the assigned interface power rather than an independent PWM/PCC measurement.

2.2. Induction Motor Transient Modeling

A third-order IM model explains the voltage–slip mechanism; the time-domain model retains the full electrical states of a single-cage SPS machine without assuming exact reduction. Magnetic saturation and stall protection are absent.

The state variables of the IM are defined as:

$$\mathbf{x}_{\mathbf{IM}} = \begin{bmatrix} E'_d & E'_q & s \end{bmatrix}^T \tag{6}$$

The states E'_d and E'_q are transient internal voltages, and s is rotor slip.

Under a synchronously rotating *dq* reference frame, with stator current positive into the motor, the transient internal-voltage dynamics are expressed as [7]:

$$\begin{aligned} \frac{dE'_d}{dt} &= -\frac{E'_d + (X_s - X')i_q}{T'_0} + s\omega_s E'_q \\ \frac{dE'_q}{dt} &= -\frac{E'_q - (X_s - X')i_d}{T'_0} - s\omega_s E'_d \end{aligned} \tag{7}$$

where T_0' is the transient open-circuit time constant, X_s and X' are the synchronous and transient reactances, i_d and i_q are the stator-current components, and $\omega_s = 2\pi f$ is the synchronous electrical angular speed in rad/s when physical time is expressed in seconds. The electrical variables are represented on a consistent motor per-unit base.

Under the same *dq* and current-direction conventions, the corresponding stator algebraic equations and electromagnetic torque relation are:

$$\begin{aligned} v_d &= E_d' + R_s i_d - X' i_q \\ v_q &= E_q' + R_s i_q + X' i_d \\ T_e &= E_d' i_d + E_q' i_q \end{aligned} \tag{8}$$

where R_s is stator resistance and T_e is electromagnetic torque on the motor per-unit base.

The mechanical dynamics are described by the torque balance equation:

$$\frac{ds}{dt} = \frac{T_m - T_e}{2H} \tag{9}$$

where H is the inertia constant in seconds, and T_m and T_e are the total opposing mechanical torque and electromagnetic torque expressed on a common per-unit torque base. The opposing torque includes the external mechanical load and viscous friction. In the implemented model, the external load torque is constant at 1850 N·m, and the viscous friction coefficient is 0.02 N·m·s. The total opposing torque is converted from $T_{\text{load}} + B\omega_m$ to per unit using the torque base $T_b = S_N / \omega_{\text{sm}}$. The inertia constant is defined as $H = J\omega_{\text{sm}}^2 / (2S_N)$, where J is the rotor inertia, S_N is the motor rated apparent power, and ω_{sm} is the synchronous mechanical angular speed. For the implemented 315 kVA motor with $J = 6\,\text{kg}\cdot\text{m}^2$ and two pole pairs at 50 Hz, $H \approx 0.235$s.

Slip is defined as:

$$\begin{aligned} s &= \frac{\omega_s - p\omega_m}{\omega_s} = 1 - \frac{\omega_m}{\omega_{\text{sm}}} \\ \omega_{\text{sm}} &= \frac{\omega_s}{p} \end{aligned} \tag{10}$$

where ω_m is mechanical rotor speed and p is the number of pole pairs, linking mechanical and electrical speed bases.

For the third-order model, reactive-power demand depends on the terminal voltage and electromagnetic states:

$$Q_{\text{IM}} = h_{\text{IM}}(V, \theta, \mathbf{x_{IM}}) \tag{11}$$

where V and θ are the terminal-voltage magnitude and angle in the adopted synchronous reference frame. The function h_{IM} is determined from the stator algebraic equations and the reactive-power relationship $Q_{\text{IM}} = v_q i_d - v_d i_q$, with positive reactive power denoting motor consumption.

Let $v_d = V\cos\theta$, $v_q = V\sin\theta$, and $D_s = R_s^2 + X'^2$. Substituting the stator algebraic equations into the reactive-power relationship gives:

$$Q_{\text{IM}} = \frac{X'\left[V^2 - v_d E_d' - v_q E_q'\right] + R_s\left[v_d E_q' - v_q E_d'\right]}{D_s} \tag{12}$$

Accordingly, linearization along the operating trajectory yields:

https://doi.org/10.3390/sym18111859

$$\Delta Q_{\mathrm{IM}} = \frac{\partial h_{\mathrm{IM}}}{\partial V}\Delta V + \frac{\partial h_{\mathrm{IM}}}{\partial \theta}\Delta \theta + \frac{\partial h_{\mathrm{IM}}}{\partial x_{\mathrm{IM}}}\Delta x_{\mathrm{IM}} \tag{13}$$

To evaluate Equation (13), let $a = E'_d \cdot \cos\theta + E'_q \cdot \sin\theta$, $b = E'_q \cdot \cos\theta - E'_d \cdot \sin\theta$, and $D_s = R_s^2 + X'^2$. With $h_z = \partial h_{IM} / \partial z$ and the other independent variables fixed, differentiation of Equation (12) gives the voltage derivatives:

$$\begin{aligned} h_V &= \frac{X'(2V - a) + R_s b}{D_s} \\ h_\theta &= -\frac{V\left(X'b + R_s a\right)}{D_s} \end{aligned} \tag{14}$$

The derivatives with respect to $\mathbf{x}_{\mathrm{IM}} = \left[E'_d, E'_q, s\right]^{\mathrm{T}}$ are:

$$\begin{aligned} h_{E_{d'}} &= -\frac{V\left(X'\cos\theta + R_s \sin\theta\right)}{D_s} \\ h_{E_{q'}} &= \frac{V\left(R_s \cos\theta - X'\sin\theta\right)}{D_s} \\ h_s &= 0 \\ \mathbf{h}_{x_{IM}} &= \left[h_{E_{d'}},\ \ h_{E_{q'}},\ \ 0\right] \end{aligned} \tag{15}$$

At a selected smooth trajectory instant t_0, Equations (14) and (15) are evaluated at $(V_0, \theta_0, E'_{d,0}, E'_{q,0}, s_0)$, where each subscript-0 quantity denotes its value at t_0. These derivatives provide the IM reactive-demand contributions to the algebraic Jacobian used in the Schur-complement reduction in Section 3.1. The other independent variables, network topology, reference phasor, converter-limit active set, and controller/filter memories are fixed during differentiation; switching instants are treated piecewise. Although $h_s = 0$, slip affects reactive demand through Equation (7). Appendix C checks all five derivatives at three explicitly specified algebraic test states.

Without saturation, thermal protection, or mechanical stopping, $s > 1$ is only a qualitative numerical non-recovery indicator; the physical scope is detailed in Section 5.5.

2.3. Network Modeling and DPV–IM Coupled DAE

A unified DAE couples converter and motor states through the feeder algebraic power balance.

For a balanced *n*-bus network, the complex nodal current and voltage vectors satisfy:

$$\mathbf{I} = \mathbf{Y}_{\mathrm{bus}}\mathbf{V} \tag{16}$$

where $\mathbf{I}$ and $\mathbf{V}$ are complex phasor vectors and $\mathbf{Y}_{\mathbf{bus}}$ is the nodal admittance matrix. For impedance-based sensitivity calculations, the source voltage is fixed and the reference bus is eliminated. Partitioning the nodal equations gives $\mathbf{I}_L = \mathbf{Y}_{LL}\,\mathbf{V}_L + \mathbf{Y}_{L0}\,\mathbf{V}_0$. The corresponding reduced impedance and voltage relationships are:

$$\begin{aligned} \mathbf{Z}_{\mathrm{red}} &= \mathbf{Y}_{LL}^{-1} \\ \mathbf{V}_L &= \mathbf{Z}_{\mathrm{red}}\left(\mathbf{I}_L - \mathbf{Y}_{L0}\mathbf{V}_0\right) \end{aligned} \tag{17}$$

The subscript L denotes nonreference buses; $\mathbf{V}_0$ is the fixed source phasor and $\mathbf{Y}_{L0}$ retains its coupling to those buses. Only the nonsingular reduced admittance is inverted [17,19].

In polar-coordinate form, the nodal voltage vector is expressed as:

$$\mathbf{V} = \left[V_1 e^{j\theta_1}, V_2 e^{j\theta_2}, \ldots, V_n e^{j\theta_n} \right]^T \tag{18}$$

where the reference-bus angle is fixed, and only nonreference-bus voltage variables are retained in the reduced algebraic system.

According to the nodal power-balance relations, the active and reactive power balances at bus *k* satisfy

$$\begin{aligned} P_k^{\mathrm{PV}} - P_k^{\mathrm{IM}} - P_k^{L} &= V_k \sum_{m=1}^{n} V_m \left(G_{km} \cos\theta_{km} + B_{km} \sin\theta_{km} \right) \\ Q_k^{\mathrm{PV}} - Q_k^{\mathrm{IM}} - Q_k^{L} &= V_k \sum_{m=1}^{n} V_m \left(G_{km} \sin\theta_{km} - B_{km} \cos\theta_{km} \right) \end{aligned} \tag{19}$$

where G_{km} and B_{km} are the real and imaginary parts of the admittance matrix, and $\theta_{km} = \theta_k - \theta_m$. Positive DPV power denotes injection, whereas IM and static-load powers denote consumption. All powers are expressed on a common network base.

The DPV powers in Equation (19) follow the voltage-dependent dq relationships in Equation (1), linking them to the separate currents in Equation (19). For the averaged interface, $P_j = S_j \cdot V_{eff,j} \cdot i_{d,j}$ and $Q_j = S_j \cdot V_{eff,j} \cdot i_{q,j}$; $i_{q,j}$ is the nonnegative reactive-support magnitude. Positive support corresponds to a negative physical q-axis current under voltage-oriented control, with its magnitude expressed on the stated site current base. These site-per-unit products include S_j once and are divided by the common network power base before substitution in Equation (19).

The retained differential states are:

$$\mathbf{x} = \left[\mathbf{x}_{\mathrm{IM}}^T, \mathbf{x}_{\mathrm{dc}}^T \right]^T \tag{20}$$

The analytical states comprise reduced motor states $\mathbf{x}_{\mathrm{IM}}$ and DC states $\mathbf{x}_{\mathrm{dc}}$, with controller states appended when retained. The SPS simulation retains its full motor electrical states.

The algebraic variables are defined as:

$$\mathbf{y} = \left[\boldsymbol{\theta}^T, \mathbf{V}^T, \mathbf{i}_{d,\mathrm{PV}}^T, \mathbf{i}_{q,\mathrm{PV}}^T \right]^T \tag{21}$$

Here $\boldsymbol{\theta}$ and $\mathbf{V}$ contain the nonreference-bus voltage angles and magnitudes, while $\mathbf{i}_{d,\mathrm{PV}}$ and $\mathbf{i}_{q,\mathrm{PV}}$ are the separate averaged-interface current variables. The latter denotes the nonnegative reactive-support magnitude; positive support corresponds to a negative physical q-axis current in Equation (1), with the magnitude converted using the stated site current base. Other auxiliary algebraic variables are collected in $\mathbf{z}$.

Therefore, the DPV–IM distribution system can be expressed as:

$$\begin{aligned} \dot{\mathbf{x}} &= \mathbf{f}(\mathbf{x}, \mathbf{y}, \mathbf{u}) \\ \mathbf{0} &= \mathbf{g}(\mathbf{x}, \mathbf{y}, \mathbf{u}) \end{aligned} \tag{22}$$

where ***f*** describes the differential dynamics, ***g*** contains the network power-balance and device algebraic equations, and $\mathbf{u}$ contains control inputs and fault conditions. Converter current limits are implemented through piecewise saturation laws rather than additional equality constraints. Local linearization is performed within a fixed active set and excludes switching instants.

For the Schur reduction in Section 3, converter-current and auxiliary algebraic variables are grouped as:

$$\mathbf{y} = \left[\boldsymbol{\theta}^T, \mathbf{V}^T, \mathbf{z}^T \right]^T \tag{23}$$

https://doi.org/10.3390/sym18111859

where **z** collects the converter-current and auxiliary algebraic variables, with the reference angle fixed before elimination.

Figure 1 summarizes the unified DPV–IM–network model established in this section.

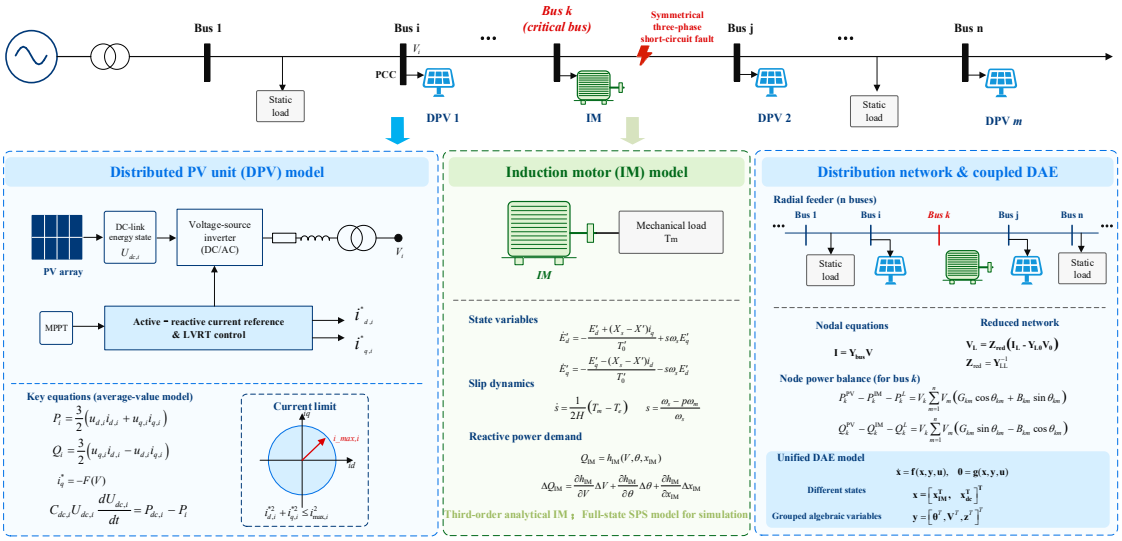


Figure 1. Unified DPV–IM–network modeling for transient voltage interaction analysis under three-phase symmetrical faults. The superscript "*" denotes a reference value.

3. Trajectory-Local Transient Voltage Dynamics and Q–V Sensitivity Analysis

3.1. Reduced Q–V Mapping via DAE Linearization

At a selected trajectory point and fixed converter active set, Equations (22) and (23) are written as:

$$\begin{aligned} \dot{\mathbf{x}} &= \mathbf{f}(\mathbf{x}, \mathbf{y}, \mathbf{u}) \\ \mathbf{0} &= \mathbf{g}(\mathbf{x}, \mathbf{y}, \mathbf{u}) \end{aligned} \tag{24}$$

where **x** comprises the retained IM, DC-link, and controller states, while the algebraic variables are organized as:

$$\mathbf{y} = \left[\boldsymbol{\theta}^T, \mathbf{V}^T, \mathbf{z}^T\right]^T \tag{25}$$

Here, $\boldsymbol{\theta}$ and **V** are the nonreference-bus voltage-angle and magnitude vectors, and **z** collects auxiliary algebraic variables. A first-order expansion of the algebraic constraints at a fixed trajectory point gives:

$$\mathbf{0} = \mathbf{G}_x \Delta\mathbf{x} + \mathbf{G}_\theta \Delta\boldsymbol{\theta} + \mathbf{G}_V \Delta\mathbf{V} + \mathbf{G}_z \Delta\mathbf{z} + \mathbf{G}_u \Delta\mathbf{u} \tag{26}$$

All Jacobian blocks use that point and active set; switching instants require separate linearizations.

Assuming that the relevant Jacobian blocks are nonsingular, the auxiliary algebraic variables and voltage-angle perturbations are sequentially eliminated through Schur-complement reduction. The resulting coefficients define the reduced Q–V Jacobian $\mathbf{J}_{QV}$ and the state-coupling matrix $\mathbf{H}x$. The reduced incremental relationship can be written as

$$\Delta\mathbf{Q} = \mathbf{J}_{QV} \Delta\mathbf{V} + \mathbf{H}_x \Delta\mathbf{x} \tag{27}$$

The equivalent forcing $\mathbf{\Delta Q}$ includes the specified active-power perturbations after elimination. Equation (27) retains angle-induced active–reactive coupling and dynamic-state dependence.

When $\mathbf{J}_{QV}$ is nonsingular, the open-loop Q–V sensitivity matrix is defined as:

$$\mathbf{Z}_Q = \mathbf{J}_{QV}^{-1} \tag{28}$$

Neglecting higher-order terms, the nodal voltage perturbation is then expressed as:

$$\Delta\mathbf{V} = \mathbf{Z}_Q(\Delta\mathbf{Q} - \mathbf{H}_x\Delta\mathbf{x}) \tag{29}$$

Column j of $\mathbf{Z}_Q$ maps an equivalent reactive forcing at bus j with states frozen, before local DPV feedback.

With independent active-power and nonmotor-state perturbations fixed, $\mathbf{\Delta Q_{IM}}$ replaces the motor contribution in $\mathbf{H}_x\mathbf{\Delta x}$ without double counting:

$$\Delta\mathbf{V} = -\mathbf{Z}_Q\Delta\mathbf{Q}_{\mathrm{IM}} + \mathbf{Z}_Q\Delta\mathbf{Q}_{\mathrm{PV}} \tag{30}$$

where $\mathbf{H_x\Delta x}$ represents the equivalent IM reactive-demand forcing and $\mathbf{\Delta Q_{PV}}$ represents controllable DPV reactive injection. Both are expressed in the nonreference-bus coordinates.

When the DPV operates within a locally differentiable regulation region, its incremental reactive-power relationship can be expressed as:

$$\Delta\mathbf{Q}_{\mathrm{PV}} = -\mathbf{K}_{\mathrm{PV}}\Delta\mathbf{V} + \mathbf{B}_u\Delta\mathbf{u}_c \tag{31}$$

Here $\mathbf{K}_{\mathrm{PV}}$ represents instantaneous algebraic voltage dependence under the specified interface model, and $\mathbf{B}_u$ maps the independent support input. In the sampled implementation, holding the 50 μs site-voltage memories fixed gives zero direct gain with respect to current network voltage. The quasi-static reconstruction instead identifies the held interface voltage with nodal voltage, giving $\mathbf{K}_{pv} = -\mathrm{diag}\left(S_j i_{q,j,0}\right)$ at PV entries. This modeled dependence is included once. Frozen voltage filters add no instantaneous control gain.

Substituting Equation (31) into Equation (30) yields:

$$\left(\mathbf{I} + \mathbf{Z}_Q\mathbf{K}_{\mathrm{PV}}\right)\Delta\mathbf{V} = -\mathbf{Z}_Q\Delta\mathbf{Q}_{\mathrm{IM}} + \mathbf{Z}_Q\mathbf{B}_u\Delta\mathbf{u}_c \tag{32}$$

Define the closed-loop correction matrix as:

$$\mathbf{M} = \mathbf{I} + \mathbf{Z}_Q\mathbf{K}_{\mathrm{PV}} \tag{33}$$

If $\mathbf{M}$ is nonsingular, the closed-loop algebraic response becomes:

$$\Delta\mathbf{V} = -\mathbf{M}^{-1}\mathbf{Z}_Q\Delta\mathbf{Q}_{\mathrm{IM}} + \mathbf{M}^{-1}\mathbf{Z}_Q\mathbf{B}_u\Delta\mathbf{u}_c \tag{34}$$

The closed-loop Q–V support sensitivity matrix is therefore defined as:

$$\mathbf{S} = \mathbf{M}^{-1}\mathbf{Z}_Q \tag{35}$$

Consequently,

$$\Delta\mathbf{V} = -\mathbf{S}\Delta\mathbf{Q}_{\mathrm{IM}} + \mathbf{S}\mathbf{B}_u\Delta\mathbf{u}_c \tag{36}$$

The entry $\mathbf{S}_{kj}$ maps additive reactive forcing at bus j to voltage at bus k with algebraic feedback closed and dynamic states fixed.

This differs from derivatives with respect to independently imposed realized Q and evolving-state finite-horizon responses. Nonsingular $\mathbf{M}$ guarantees a local algebraic mapping, not dynamic stability.

https://doi.org/10.3390/sym18111859

3.2. Spatial Propagation of DPV Reactive Support

For critical bus *k*, Equation (36) can be written componentwise as:

$$\Delta V_k = -\sum_{m\in\Omega_{\mathrm{IM}}} S_{km}\Delta Q_{\mathrm{IM},m} + \sum_{j\in\Omega_{\mathrm{PV}}} S_{kj}\Delta Q_{c,j} \tag{37}$$

where Ω_{IM} and Ω_{PV} denote the IM and DPV bus sets, respectively. Here, $\Delta Q_{c,j}$ is the additive reactive-power command component represented by $\mathbf{B}_u\Delta\mathbf{u}_c$, rather than the total realized DPV reactive-power increment. The motor term represents the equivalent state-dependent forcing defined in Section 3.1.

For a radial network represented by series branch impedances, with a fixed source and negligible shunt admittances, the reduced impedance matrix admits a shared-path interpretation. The self-impedance at bus j is:

$$[\mathbf{Z}_{\mathrm{red}}]_{jj} = \sum_{\ell\in\mathcal{P}_{o,j}} Z_\ell \tag{38}$$

while the mutual impedance between buses j and k is:

$$[\mathbf{Z}_{\mathrm{red}}]_{jk} = \sum_{\ell\in\mathcal{P}_{o,j}\cap\mathcal{P}_{o,k}} Z_\ell \tag{39}$$

where $\mathcal{P}_{0,j}$ denotes the path from the source to bus *j*, and Z_ℓ is the series impedance of branch ℓ.

Common-path impedance explains structural coupling, while operating voltage, power coupling, load characteristics, and interface feedback determine the actual Q–V response.

To quantify the location-dependent effectiveness of DPV reactive support, the sensitivity from an additive reactive-power command at site j to the voltage at critical bus *k* is defined as:

$$\eta_{k,j} = \left.\frac{\partial V_k}{\partial Q_{c,j}}\right|_{\mathbf{x},\mathcal{A}} = S_{kj} \tag{40}$$

where $\mathcal{A}$ denotes the fixed converter-limit active set. The equality holds when the supplementary command is expressed as an additive reactive-power input on a consistent system base.

A larger positive $\eta_{k,j}$ indicates a larger instantaneous critical-bus voltage response to the same additive reactive-power command under the stated linearization conditions.

Consider two DPV sites j_1 and j_2 providing equal additive reactive-power commands:

$$\Delta Q_{c,j_1} = \Delta Q_{c,j_2} \tag{41}$$

Their corresponding critical-bus voltage responses satisfy

$$\frac{\Delta V_{k,j_1}}{\Delta V_{k,j_2}} = \frac{S_{k,j_1}}{S_{k,j_2}} \tag{42}$$

provided the denominator is nonzero, the applied increments are sufficiently small, and both responses are evaluated at the same operating point and active set.

If:

$$S_{k,j_1} \neq S_{k,j_2} \tag{43}$$

equal nonzero reactive-power commands produce different incremental voltage responses at the critical bus. Therefore, identical reactive-power capability does not necessarily imply identical voltage-support effectiveness.

For candidate sites with positive support sensitivities, a normalized spatial sensitivity index is defined as:

$$\hat{\eta}_{k,j} = \frac{\eta_{k,j}}{\max\limits_{m\in\Omega_{\mathrm{PV}}} \eta_{k,m}}, \quad 0 < \hat{\eta}_{k,j} \le 1 \tag{44}$$

Positive sensitivities are normalized by their maximum, not their sum. Equation (44) expresses relative local effectiveness, not optimal allocation; nonpositive gains are excluded from this ranking.

The normalized sensitivities characterize location-dependent support effectiveness across candidate DPV buses. The implemented fixed site participation coefficients follow the same unsaturated spatial ranking, with site-specific current bases accounted for, but are prescribed controller parameters rather than exact evaluations of Equation (44) or online sensitivity updates.

Power- and current-input derivatives require matching input maps. For additive terminal-Q forcing, Equation (40) gives $g_{i,j} = \eta^{\mathrm{add}}_{30,j} S_j V_{j,0}$. For the implemented equivalent post-slew Q-command input with its local voltage filter frozen, $g_{i,j} = \eta^{\mathrm{cmd}}_{30,j} S_j V_{f,j,0}$. The two forms coincide only when their voltage references and input definitions coincide. With an actual voltage-memory state held, its held voltage replaces nodal voltage in the current-input map. Ratings use a common power base; current commands retain site-rated bases. Quasi-static and held-voltage phasor checks are distinguished from finite-horizon dynamics in Section 5.4.

Topology, capacity, operating point, and active constraints can change the sensitivities; Section 4.1 outlines a possible recalculation, while the implementation retains fixed coefficients.

Section 5.4 separately checks reconstructed frozen-P/Q algebraic predictions and evolving-state spatial responses.

3.3. Transient Recovery Boundary Under Converter Saturation and IM Dynamics

Under severe sags, current limits restrict additional support while motor slip evolves, making recovery depend on converter capability and motor re-acceleration.

For the *j*-th DPV, the converter current must satisfy:

$$i_{d,j}^2 + i_{q,j}^2 \le I_{\max,j}^2 \tag{45}$$

where $I_{\max,j}$ is the applicable converter current limit on its rated-current base.

At an active current limit, a larger request need not increase realized current. Reactive power still depends on voltage and active-current redistribution, so the unsaturated ranking need not persist.

Meanwhile, the IM recovery process is governed by its mechanical state. From Equation (9), the slip dynamics satisfy:

$$\frac{ds}{dt} = \frac{T_m - T_e}{2H} \tag{46}$$

Here, T_m includes load and friction torque; re-acceleration requires sustained excess electromagnetic torque. A temporary voltage rebound alone does not establish motor recovery.

Based on these characteristics, transient recovery is evaluated using both the critical-bus voltage and IM slip.

The voltage-recovery condition is defined as:

$$V_k(t) \geq V_{\text{rec}}, \quad t \in [t_r, t_r + T_{\text{hold}}] \tag{47}$$

where V_{rec} is the voltage threshold, t_r is the beginning of a qualifying post-fault recovery interval, and T_{hold} is the required continuous holding duration.

The IM recovery condition is expressed as:

$$\left|s(t_f) - s_0\right| \leq \varepsilon_s, \quad s_{\max} < s_{\text{th}} \tag{48}$$

where s_{max} is the maximum slip over the specified evaluation interval, sth is the slip screening threshold, s_0 is the corresponding pre-fault slip, t_f is the final evaluation time, and ε_s is the final-slip tolerance.

Accordingly, joint transient recovery is defined by:

$$\mathcal{C}_{\text{st}} = \begin{cases} V_k(t) \geq V_{\text{rec}} \\ s_{\max} < s_{\text{th}}, \\ \left|s(t_f) - s_0\right| \leq \varepsilon_s \end{cases} \tag{49}$$

Equation (49) combines sustained voltage recovery with the motor-state screening conditions. In the case studies, $V_{\text{rec}} = 0.9\,p.u.$, $T_{\text{hold}} = 100$ ms, $S_{\text{th}} = 0.5$, and $\varepsilon_s = 0.002$. The numerical criteria and observation windows are specified in Section 5.

Equation (49) is a finite-horizon recovery screen rather than a Lyapunov certificate or universal stalling boundary. Section 5 distinguishes opening commands from extinction times and treats $s > 1$ trajectories only as qualitative numerical non-recovery indicators.

4. Proposed Coordinated Transient Voltage Support Strategy

Figure 2 illustrates CTVS. Critical-bus voltage magnitude, voltage-decrease rate, and motor slip form a common support signal, distributed through fixed site coefficients. The local stage applies reactive-current priority, assigns the residual current capability to active power, and adjusts the active request through DC-link feedback.

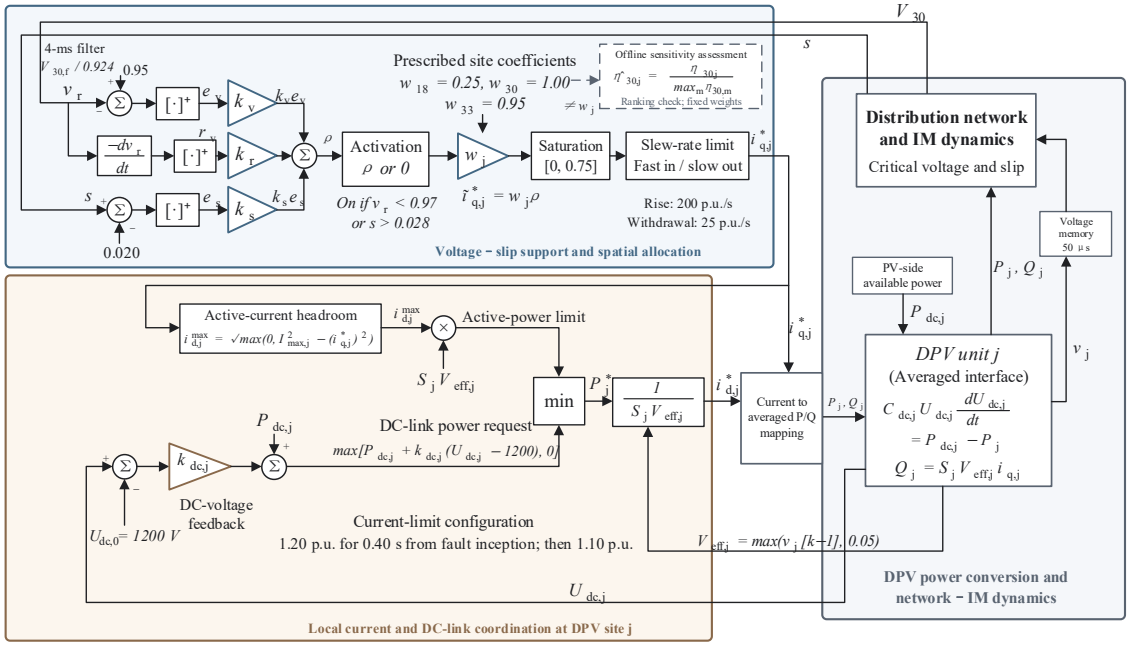


Figure 2. Schematic diagram of the proposed CTVS control architecture and local converter–DC-link coordination.

4.1. Spatial Weighting and Reactive-Current Allocation

The local sensitivities in Equations (40) and (44) motivate location-dependent support coefficients.

For a common per-unit support signal $\rho(t)$, the preliminary reactive-current reference at site *j* is:

$$\tilde{i}_{q,j}^{*}(t) = w_j \rho(t) \tag{50}$$

Here w_j is prescribed and the tilde denotes the unsaturated reference. The nonnegative support current $i_{q,j}^{*}$ is opposite to the signed physical *q* current. Site-specific bases mean Equation (50) scales a common signal rather than allocating a fixed total current or Q.

The local reactive-current limit gives:

$$i_{q,j}^{*}(t) = \min\left\{ w_j \rho(t), i_{q,\lim,j} \right\} \tag{51}$$

where $i_{q,\lim,j}$ denotes the allowable reactive-current target. In the implemented controller, the supplementary reactive-current target is capped at 0.75 p.u. and remains subject to the converter current-circle constraint. Saturated requests are not redistributed to other sites.

For critical Bus 30, the CTVS controller uses prescribed fixed participation coefficients of 0.25 at Bus 18, 1.00 at Bus 30 (unit participation reference), and 0.95 at Bus 33. Rather than representing online evaluations of Equation (44) or a global optimization solution, these fixed constants reflect the unsaturated spatial-support priority across the three sites and remain constant throughout the formal CTVS tests. Section 5.4 provides both frozen-state algebraic checks and finite-horizon dynamic perturbation tests to quantify the local support efficiency of these prescribed coefficients relative to analytical sensitivity weights and uniform allocation.

Following a topology or capacity change, updated network parameters, operating-point information, active constraints, and site bases would permit recalculation and normalization of the local sensitivities before revising the coefficients. This is a possible extension; the tested controller retains fixed coefficients and implements no online update.

4.2. Voltage–Slip Coordinated Dynamic Regulation

Because voltage recovery can precede IM re-acceleration, CTVS combines the critical-bus voltage deficit, voltage-decrease rate, and slip deviation to determine the required reactive-current support.

The CTVS critical-bus voltage uses a first-order filter with a 4 ms time constant. Its normalized control signal is $v_r = \dfrac{V_{30,f}}{0.924}$, where $V_{30,f}$ is the filtered absolute Bus-30 voltage in p.u. and 0.924 p.u. is a fixed control reference, rather than the measured pre-fault voltage. The thresholds 0.95 and 0.97 apply to this normalized signal; the 0.90-p.u. recovery criterion in Section 5 applies to the absolute bus voltage. The site-voltage filters use a 2 ms time constant. The voltage deficit is defined as:

$$e_v(t) = \left[0.95 - v_r(t) \right]_{+} \tag{52}$$

where $\left[x \right]_{+} = \max(x, 0)$. The voltage-channel gain is $k_v = 4$.

The one-sided voltage-decrease rate is defined as:

$$r_v(t) = \left[-\frac{dv_r(t)}{dt} \right]_+ \tag{53}$$

Filtering precedes differentiation; $r_v(t)$ vanishes when voltage stops falling. Because $r_v(t)$ has units p.u./s, k_r has the time dimension required for a per-unit current contribution.

The slip deviation is expressed as:

$$e_s(t) = [s(t) - 0.020]_+ \tag{54}$$

where 0.020 is the control reference for motor slip, distinct from the measured pre-fault slip s_0 used in the recovery assessment. The slip-channel gain is $k_s = 9$.

The combined support signal is:

$$\rho(t) = k_v e_v(t) + k_s e_s(t) + k_{rv} r_v(t) \tag{55}$$

With the adopted gains, Equation (55) becomes:

$$\rho(t) = 4e_v(t) + 9e_s(t) + 0.008 r_v(t) \tag{56}$$

Slip feedback sustains support after voltage rebounds while the motor is still re-accelerating.

Supplementary support is activated when either condition holds:

$$v_r < v_{\text{trig}} \quad \text{or} \quad s > s_{\text{trig}} \tag{57}$$

where $v_{\text{trig}} = 0.97$ p.u. and $s_{\text{trig}} = 0.028$. When neither condition is satisfied, the supplementary reactive-current target returns toward zero through the withdrawal rate limit.

After spatial scaling and target saturation, an asymmetric rate limiter shapes the reactive-current command:

$$-i_{q,\text{down}} \le \frac{di_{q,j}^*}{dt} \le i_{q,\text{up}} \tag{58}$$

The positive rise and withdrawal rates are:

$$\begin{aligned} i_{q,\text{up}} &= 200\text{p.u./s} \\ i_{q,\text{down}} &= 25\text{p.u./s} \end{aligned} \tag{59}$$

Fast entry and slower withdrawal support motor re-acceleration; final current feasibility is enforced afterward.

The overall execution sequence, from signal triggering to current-command generation, is illustrated in Figure 3.

4.3. Converter Current and DC-Link Coordination

The local stage applies reactive priority and DC feedback within the residual active-current capability.

The converter current references at site *j* satisfy:

$$\left(i_{d,j}^*\right)^2 + \left(i_{q,j}^*\right)^2 \le i_{\max,j}^2 \tag{60}$$

where $i_{\max,j}$ is the applicable current limit on the site-rated current base. Under reactive-current priority, the remaining active-current capability is:

$$i_{d,j}^{\max} = \sqrt{\max\left[0, i_{\max,j}^2 - \left(i_{q,j}^*\right)^2\right]} \tag{61}$$

https://doi.org/10.3390/sym18111859

For the fair-condition comparisons, all controllers use the same fault-triggered current-limit schedule: 1.20 p.u. during the first 0.40 s after fault inception and 1.10 p.u. thereafter. The overload timer is referenced to fault inception rather than accumulated controller activation time.

Increasing reactive current reduces the current margin available for active-power transfer. Figure 4 illustrates the corresponding operating points.

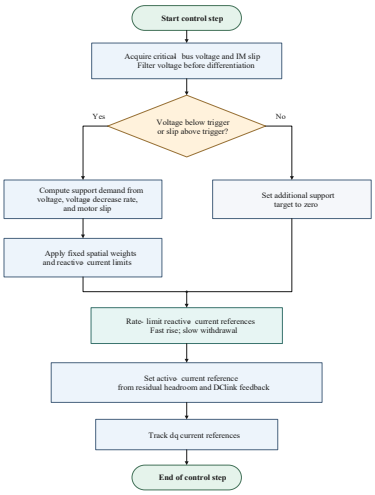


Figure 3. Flow chart of the proposed CTVS.

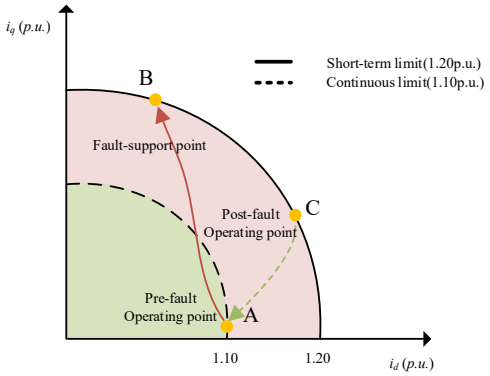


Figure 4. Schematic converter-current operating points during fault support and recovery.

The active-power reference is limited by the residual AC capability:

$$P_j^* = \min\left\{\max\left\{P_{\mathrm{dc},j} + k_{\mathrm{dc},j}(U_{\mathrm{dc},j} - U_{\mathrm{dc0},j}), 0\right\}, S_j V_{\mathrm{eff},j}, i_{d,j}^{\max}\right\} \tag{62}$$

where $P_{dc,j}$ is the available DC-side power, $U_{dc,j}$ and $U_{dc,0}$ are the actual and nominal DC-link voltages, $k_{dc,j}$ is the DC-voltage feedback gain, S_j is the site-rated apparent power, and v_j is the per-unit PCC voltage.

Positive DC deviation increases the active request within the remaining AC capability. Any excess DC input still charges the capacitor; Equation (62) cannot enforce a hard DC-voltage ceiling.

The active-current reference is calculated as:

$$i_{d,j}^* = \frac{P_j^*}{S_j V_{\mathrm{eff},j}} \tag{63}$$

The implemented guard is $V_{\mathrm{eff},j} = \max\{v_j, 0.05\}$, and the inner maximum in Equation (62) enforces nonnegative active power. Neither is an additional protection device.

The DC-link dynamics are expressed as:

$$C_{\mathrm{dc},j} U_{\mathrm{dc},j} \frac{dU_{\mathrm{dc},j}}{dt} = P_{\mathrm{dc},j} - P_j \tag{64}$$

where $C_{dc,j}$ is the DC-link capacitance and P_j is the active power enforced by the averaged AC interface after the applicable command limits. The stored-energy variation is determined by the resulting input–output power imbalance.

The 1320 V assessment threshold triggers no hardware protection. The 900–1600 V numerical bounds do not represent physical dissipation; Section 5.3 separates their energy corrections from unclamped compliance.

The corresponding active- and reactive-power responses during LVRT and recovery are illustrated in Figure 5. The time labels t_1 and t_2 denote fault inception and the programmed fault-opening command, respectively; the latter is distinguished from the actual current-zero extinction instant.

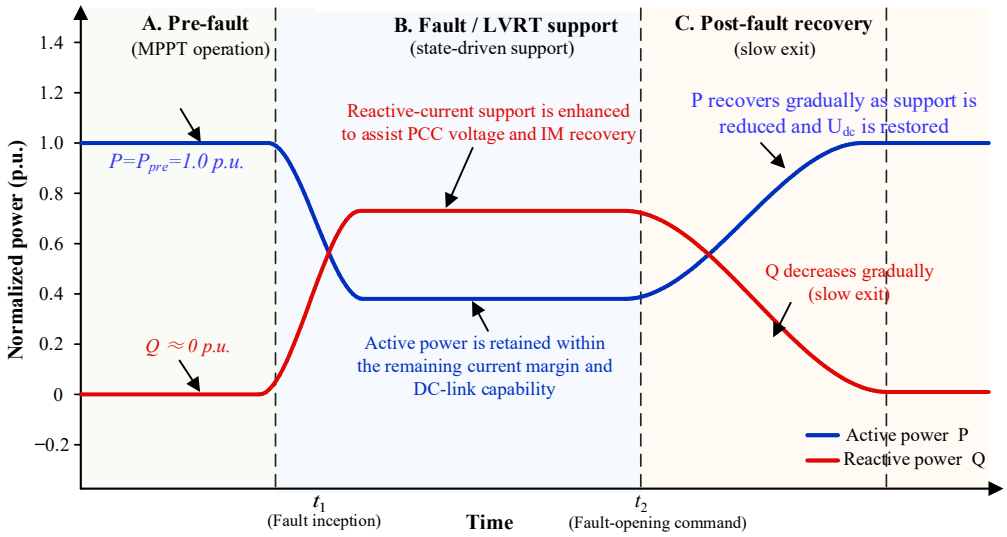


Figure 5. Active- and reactive-power responses of DPVs during LVRT and recovery dynamics.

5. Case Study

5.1. Simulation Setup and Evaluation Criteria

The modified IEEE 33-bus feeder in Figure 6 integrates three averaged-model DPV units at Buses 18, 30, and 33 and a full-state single-cage SPS induction motor at critical Bus 30 (rated at 315 kVA, 400 V, 50 Hz, operating near 300 kW in the evaluated pre-fault conditions). Table 1 summarizes the common system and controller settings. Appendices A and C provide the equivalent-circuit, transformer, source, complete modified feeder, initialization, and numerical implementation data. The validation concerns the specified Bus-32 three-phase faults; other fault locations, feeder topologies, and unbalanced faults are outside the demonstrated scope.

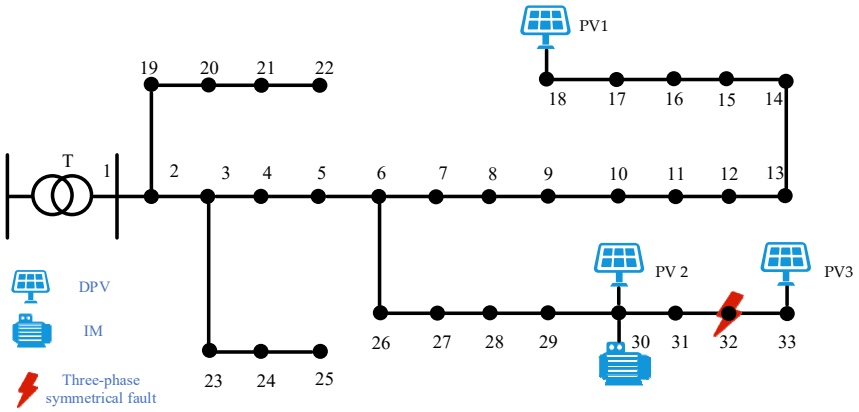


Figure 6. Configuration of the modified IEEE 33-bus test feeder with DPV units and IM load.

A 4.0 s initialization warm-up precedes fault inception at physical time $t_{on} = 4.0$ s (displayed time axes are shifted by 3.8 s so that fault inception appears at 0.20 s). The programmed fault duration d specifies the opening command $t_{cmd} = t_{on} + d$. Because circuit-breaker interruption occurs at phase-current zeros and individual phase-extinction instants are not separately logged, post-fault recovery delays are referenced consistently to t_{cmd}. Over the pre-fault interval [3.8, 4.0) s, the matched controllers share the same initialized pre-fault condition, with a reported mean Bus-30 voltage of 0.918778 p.u. and a mean motor slip of 0.017164.

Corrected Local LVRT (incorporating the unified overload schedule and filtered derivative), literature-inspired Adaptive Q–V Droop [22], and Full CTVS share the identical physical plant, initialization, DC-link feedback, current-circle limit, slew-rate limit, and fault-triggered overload schedule from t_{on}. Their reactive-current reference generation differs: Local LVRT differentiates the 2 ms filtered site voltage; CTVS uses its 4 ms critical-bus channel normalized by the fixed reference 0.924 p.u. ($v_r = V_{30,f} / 0.924$). The CTVS thresholds 0.95/0.97 act on normalized vr, whereas Local's 0.95 threshold and the 0.90-p.u. recovery screen use absolute site/bus voltages. All controller gains remain fixed across the principal comparisons, ablations, boundary scans, and IM-parameter cases. Only the explicitly labeled local gain-sensitivity check in Section 5.5 varies k_v or k_s.

Table 1. Key System, Machine, and Controller Parameters.

Category/Component	Parameter Settings	Description/Remarks
System/loads	IEEE 33-bus; 12.66 kV; 50 Hz; 1.0 MVA base; nominal-P/Q RLC impedances	Feeder p.u.; complete branch/load data in Table A5
Source	Active short-circuit level 100 MVA; X/R = 7	Exact R/X/L in Table A1
DPV sites/inputs	Buses 18/30/33; S = 0.20/0.45/0.35 MVA; P_{dc} = 196/441/343 kW	Site current bases; imposed DC input
IM	Bus 30; single-cage SPS; 315 kVA, 400 V, 50 Hz	Full electrical states; circuit in Table A1
IM mechanics	J = 6; p = 2; H = 0.2350; external T_{load} = 1850; B = 0.02	kg m²; pole pairs; s; N m; N m s
Transformer	500 kVA; 12.66/0.4 kV; D1/Yg	Winding/core values in Table A1
DC link	C_{dc} = 0.20/0.45/0.35; $U_{dc,0}$ = 1200; k_{dc} = 500/1125/875	F; V; W/V; averaged P/Q interface

DC bounds	1320 assessment; 900–1600 numerical interval	V; neither is hardware protection
CTVS gains	k_v = 4; k_s = 9; k_r = 0.008; slip reference 0.020; trigger 0.028	Fixed gains; rate channel uses p.u./s
Spatial coefficients	Full: 0.25/1.00/0.95; Uniform: 0.8325	Prescribed; capacity-weighted nominal match
Voltage channels	Critical: 4 ms, fixed reference 0.924; site/Local: 2 ms	CTVS 0.95/0.97 act on normalized vr
Corrected Local	k = 1.5; Vth = 0.95; k_{dv} = 0.02	Actual filtered-voltage derivative, p.u./s
Adaptive Droop	Deadband 0.03; saturation drop 0.30; floor 0.10; Psched filter 20 ms	Reactive branch only; law in Section 5.3
Current/slew	1.20 for 0.40 s from fault inception, then 1.10; rise/withdraw 200/25; CTVS/Droop target cap 0.75	Site p.u.; p.u./s; target cap ≠ circle limit
Fault/solver	Bus 32; three-phase; 8 Ω; t_{on} = 4.0 s after 4 s warm-up; ode3/Backward Euler; 50 μs	Opening command ton + d; common timing
Recovery screen	Absolute $V \geq 0.90$ for 100 ms; $s_{max} <$ 0.5; final-slip error ≤ 0.002; TVSI 1 s; joint endpoint 3 s	Delays/windows from opening command

Static feeder loads are modeled as three-phase RLC impedance branches specified by their nominal 50 Hz active and reactive powers, rather than ideal constant-power sinks during transients. The extracted bus-load records sum to 3745 kW and 2310 kvar before the additional 20 kW Load34 block at Bus 33 and the three 1 W DPV interface shunts, giving a total nominal static load of 3765.003 kW and 2310 kvar; the IM is modeled separately. The feeder retains the IEEE 33-bus topology, while the implemented branch and load parameters are those of the saved modified model.

Recovery delays start at t_{cmd}. First crossing is the first sample at or above 0.90 p.u. after the opening command, with zero delay if already above it. Sustained recovery starts at the earliest qualifying 100 ms interval, including both endpoints; the holding interval is not added to the delay. TVSI uses a fixed 1 s post-command window:

$$TVSI_{1\mathrm{s}} = \int_{t_{\mathrm{cmd}}}^{t_{\mathrm{cmd}}+1\cdot\mathrm{s}} \max\left\{0, 0.90 - V_{30}(t)\right\} dt \tag{65}$$

Joint recovery at $t_{end} + 3s$ requires sustained voltage recovery, maximum slip below 0.5 from fault inception to that endpoint, and final slip error within 0.002 of prefault mean. The original displayed window ends at physical 5.0 s (aligned 1.20 s); extended evaluations end at $t_{end} + 3s$.

The thresholds assess motor deceleration and sustained voltage restoration. The 0.90-p.u. level lies below the measured pre-fault Bus-30 voltage of 0.918778 p.u., and the 100 ms hold spans five 50 Hz cycles to reject temporary voltage rebounds. A slip tolerance of 0.002 corresponds to 0.314 rad/s (3 r/min) on the 157.080-rad/s synchronous mechanical-speed base. The maximum-slip requirement of less than 0.5 requires motor speed to remain above half the synchronous mechanical speed from fault inception to the evaluation endpoint. Including the fault interval captures severe excursions even if the motor later recovers. In the adverse cases of Section 5.5, the slip screen is violated before slip exceeds 1 and before subsequent numerical DC clipping.

Metrics were recalculated from 18 retained MAT cases at 140, 145, 147, and 148 ms, varying voltage threshold (0.89/0.90/0.91 p.u.), hold (80/100/120 ms), or final-slip tolerance (0.001/0.002/0.003) one at a time. Joint classifications were unchanged in both windows.

At 140 ms, Local/Droop/Full sustained delays were 23.05/22.65/22.60 ms at 0.89 p.u., 342.30/390.85/23.85 ms at 0.90 p.u., and 443.50/475.60/389.15 ms at 0.91 p.u. Timing therefore depends on the voltage criterion; TVSI retains its 0.90 p.u. deficit and fixed 1 s integration window. The model limitations in Sections 5.3 and 5.5 and Appendix A still apply.

5.2. DPV-IM Transient Interaction and Controller Ablation

At 140 ms, Voltage-only and Full CTVS differ only in slip feedback; Uniform retains voltage–slip feedback but replaces the site coefficients. The same plant, initialization, converter limits, timing, slew, and DC implementation isolate these reference-generation changes.

Voltage-only withdraws support before motor recovery and permits a secondary voltage depression. Sustained delays are 397.45 ms (Voltage-only), 23.80 ms (Uniform), and 23.85 ms (Full); maximum slips are 0.13251/0.13112/0.13121. Their equal current envelope attributes the sustained-recovery benefit to slip-conditioned persistence, not extra current headroom.

Uniform = 0.8325 is the 0.20/0.45/0.35 capacity-weighted mean of the fixed site coefficients, matching the nominal capacity-weighted reactive-current request prior to terminal-voltage conversion and current saturation. Under the severe 140 ms fault, the Uniform and Full CTVS recovery trajectories nearly coincide under the same current-limit schedule; Figure 7d shows their common maximum-site-current envelope. The matched comparison identifies slip-conditioned support persistence as the main sustained-recovery contribution, without a separately resolved recovery benefit from the prescribed spatial coefficients. A common total-current ceiling does not imply identical reactive-power injection at each site, as reflected by the lower post-fault fleet reactive-power curve for Full CTVS in Figure 7c.

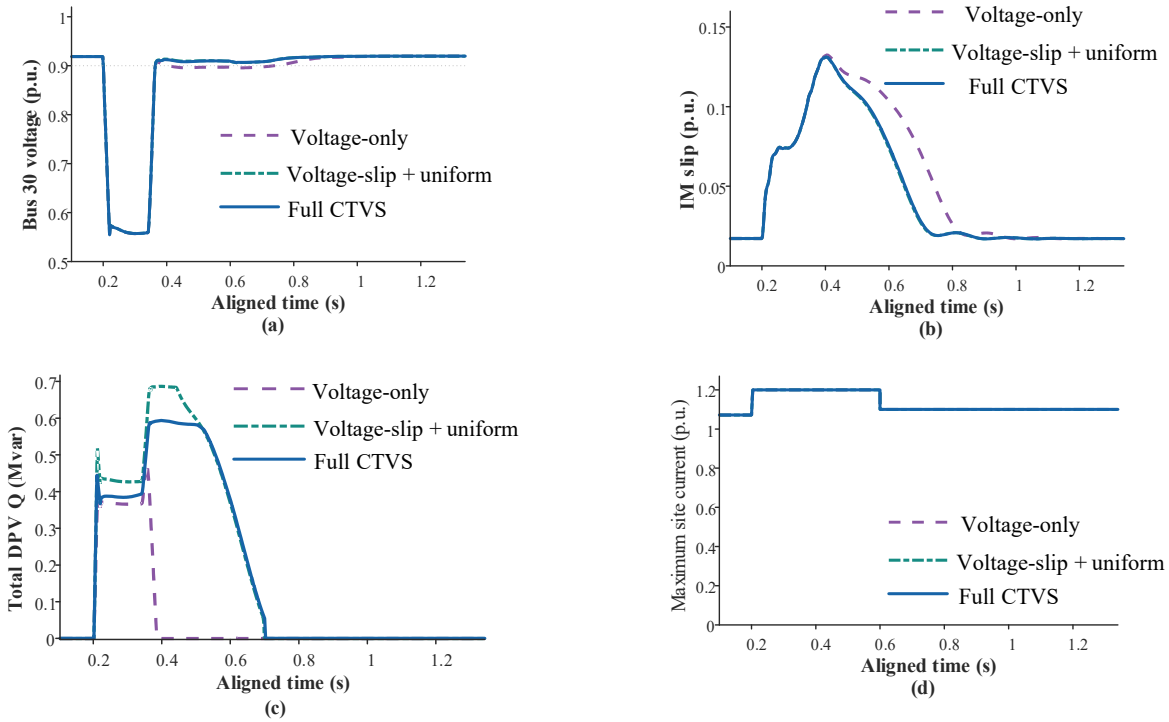


Figure 7. Ablation comparison of CTVS variants under an 8 Ω, 140 ms fault at Bus 32: (**a**) Bus-30 voltage; (**b**) IM slip; (**c**) total DPV reactive power; and (**d**) maximum converter current.

The 100 ms case provides a counterexample to a universal controller ranking. All three ablation variants jointly recover. Sustained recovery is 24.65 ms for Voltage-only, 24.40 ms for Uniform, and 24.50 ms for Full CTVS; their fixed 1 s TVSI values are 0.004591, 0.004580, and 0.004586 p.u. s. In the principal comparison, Corrected Local recovers continuously in 50.20 ms with a TVSI of 0.004679 p.u. s, but its maximum slip, 0.078723, is lower than Full CTVS's 0.079122. Full CTVS is therefore not best in every metric, and the 140 ms benefit is interpreted as disturbance-dependent.

To illustrate the physical influence of DPV electrical distance on critical-bus support with total capacity held constant, Figure 8 compares three 1 MW placement configurations—a remote single site at Bus 18, the three-site distributed fleet, and a local single site at Bus 30—under an 8-ohm, 100 ms Bus-32 fault. This separate baseline placement experiment uses its own implementation and is not pooled with the fixed-topology fair-condition controller benchmark.

For the baseline placement trajectories in Figure 8, the 0.90-p.u. voltage-recovery delays are 23.4, 111.7, and 290.9 ms for the Bus-30, three-site distributed, and Bus-18 deployments, respectively. Deployment at critical Bus 30 provides stronger voltage support despite a smaller reactive-power excursion than remote Bus 18, confirming that feeder impedance coupling governs spatial support effectiveness; this placement comparison motivates the sensitivity analysis in Section 5.4 and is kept distinct from the fixed-topology controller ablations. These baseline delays are not substituted for the sustained-recovery metric with a 100 ms hold used in the fair-condition controller comparison.

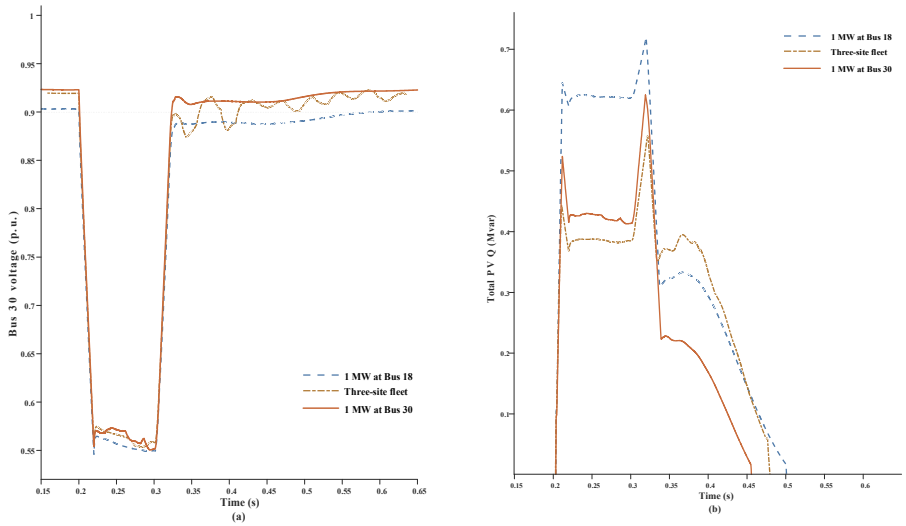


Figure 8. Impact of 1 MW DPV spatial placement under an 8 Ω, 100 ms fault at Bus 32: (**a**) Bus-30 voltage and (**b**) total DPV reactive power.

5.3. Comparative Performance and Recovery Boundary

The principal benchmark uses the fixed three-site model and an 8-ohm, 140 ms Bus-32 fault. The physical and converter conditions are shared as specified in Section 5.1; controller-specific reference generation is retained. Adaptive Q–V Droop uses the positive relative drop from each site's measured healthy filtered voltage. Its gain $K_{d,j} = Q_{\text{avail},j} / (0.30 - 0.03)$ uses $Q_{\text{avail},j} = \sqrt{\max\left(0, S_j^2 - P_{\text{sched},j}^2\right)}$, where $P_{\text{sched},j}$ is the causal 20 ms estimate of the preceding active-power command. The reactive reference is the smaller of $Q_{\text{avail},j}$ and K_{dj} times the positive excess drop above 0.03; the support-current request divides it by S_{j} times the larger of filtered site voltage and 0.10 p.u. The shared slew and current-circle limits act afterward. This adapts only the reactive-voltage branch

of Owais and Javed Iqbal [22], not their VSG, fuzzy-frequency, or PV-reserve architecture. The deadband, saturation drop, and division guard were prescribed before the benchmark; 90- and 110 ms feasibility checks confirmed operation without selecting gains from the 140 ms ranking.

All three methods jointly recover in Table 2, with first voltage crossings separated by less than 1 ms. Under the 0.90-p.u./100 ms criterion, secondary voltage depressions interrupt the holding interval for Local LVRT and Adaptive Droop, yielding sustained delays of 342.30 and 390.85 ms, versus 23.85 ms for Full CTVS, which also has a lower 1 s TVSI. For this 140 ms comparison, lowering the threshold to 0.89 p.u. (below the secondary-depression trough in Figure 9a) gives sustained recovery at approximately 23 ms for all three methods; raising it to 0.91 p.u., closer to the 0.918778 p.u. prefault voltage after support withdrawal begins, increases all three delays and reduces the timing advantage (Section 5.1).

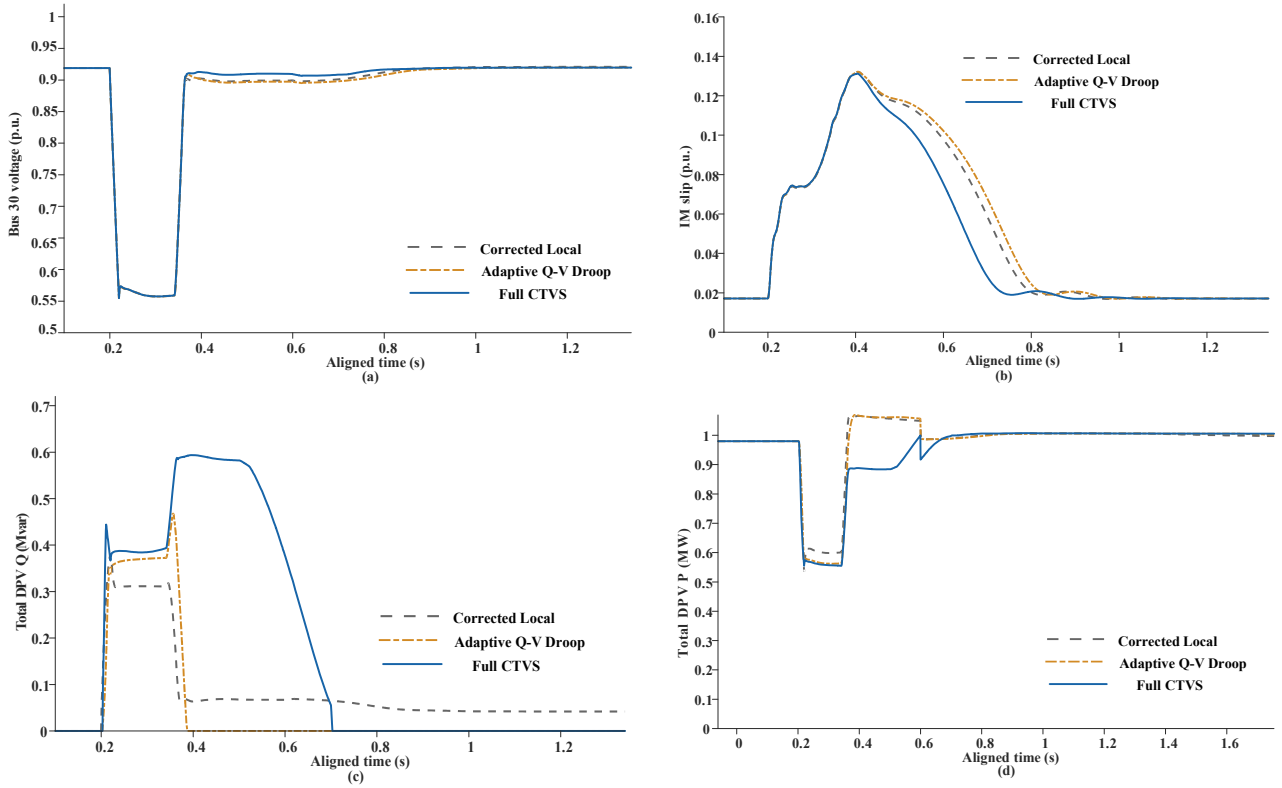


Figure 9. Dynamic responses of different control strategies under an 8 Ω, 140 ms fault at Bus 32: (**a**) Bus-30 voltage; (**b**) IM slip; (**c**) total DPV reactive power; and (**d**) total DPV active power.

Table 2. Comparison of Transient Recovery Metrics Under the 140 ms Fault.

Control Strategy	First Crossing (ms)	Sustained Recovery (ms)	TVSI$_{1s}$ (p.u.·s)	Peak Slip s_{max} (p.u.)	Peak U_{dc} (V)	Joint Recovery
Corrected Local LVRT	24.80	342.30	0.004884	0.132159	1259.7	Pass
Adaptive Q-V Droop	24.00	390.85	0.005496	0.132192	1262.1	Pass
Full CTVS	23.85	23.85	0.004511	0.131213	1282.5	Pass

The maximum-slip improvement is small. Longer reactive support and greater transient active curtailment raise CTVS's DC peak to 1282.45 V, versus 1259.70/1262.12 V for

Local/Droop. The advantage is sustained voltage recovery with an associated DC-energy cost.

The commanded fault duration is then varied without changing controller parameters. Figure 10 reports maximum slip, sustained voltage recovery for jointly recovered cases, and the joint classification for all five control variants. Voltage and motor criteria are evaluated separately before forming the joint result.

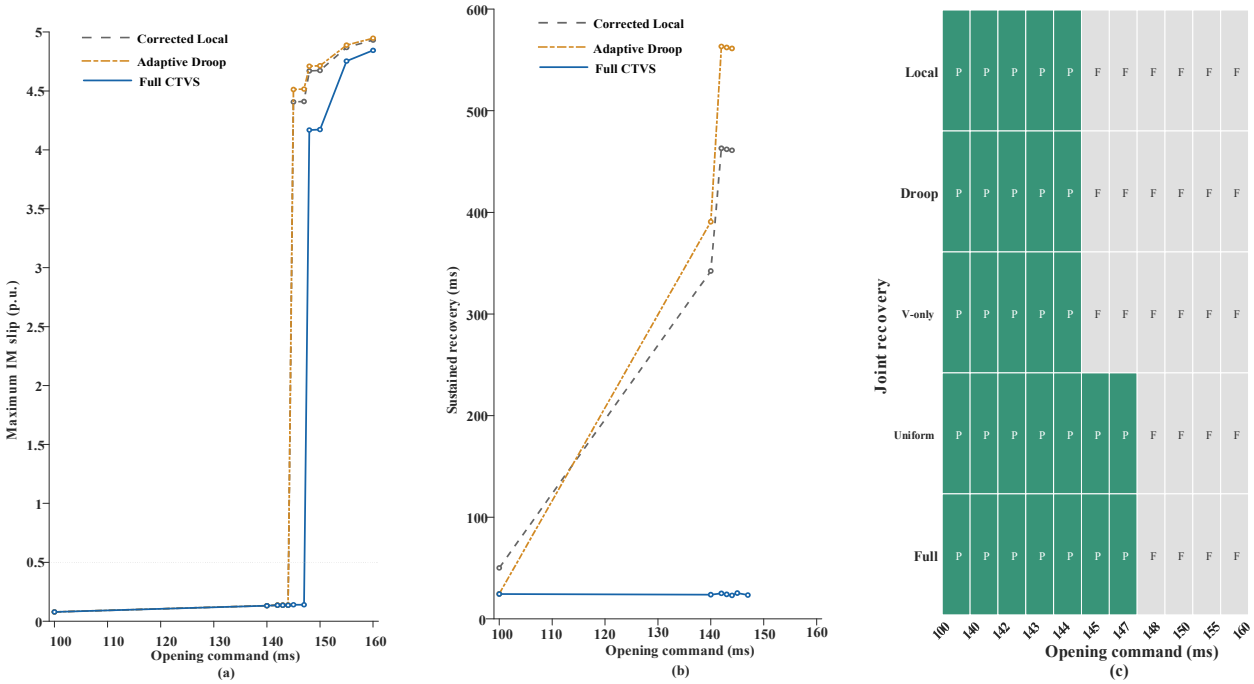


Figure 10. Transient recovery performance across fault-clearing command durations: (**a**) maximum IM slip; (**b**) sustained voltage-recovery delay; and (**c**) joint recovery classification (P: pass; F: fail).

Corrected Local, Adaptive Droop, and Voltage-only CTVS pass at the tested 144 ms command and fail at 145 ms. Voltage-Slip CTVS with uniform weights and Full CTVS pass at 147 ms and fail at 148 ms. The matched boundary of the latter two variants is consistent with the near-overlap in Figure 7 and does not support a measurable boundary gain from the prescribed spatial weights.

These brackets describe tested opening commands, not exact physical CCT. Some 145/147 ms commands produce identical sampled trajectories, consistent with current-zero interruption; last-phase extinction was not logged. Voltage recovery without motor recovery is failure. Where DC later clips, the earlier slip-screen violation establishes model failure, while the subsequent trajectory cannot quantify physical behavior. The corresponding site-level reactive-power, converter-current, and DC-link voltage trajectories under Full CTVS for the 140 ms fault are shown in Figure 11.

In the unclamped 140 ms case, current remains within its common envelope and maximum DC voltage is 1282.45 V, below the 1320 V assessment level. The energy audit spans t_{on} to t_{cmd} + 3 s, using updates on the half-open interval and capacitor states at its endpoints: P_{dc} is imposed DC input and P_{ac} is enforced average-interface output. Integrating $P_{dc} - P_{ac}$ and accounting for the explicit-Euler correction matches capacitor-energy change with residuals below 1.3×10^{-8} J. Complete station values are retained in Table A2; this checks the implemented average model, not measured converter losses.

The 1320 V level triggers no protection. Under Full CTVS at the 160 ms opening command, all sites reach the 1600 V numerical bound; the removed clamp energy has no corresponding physical dissipation circuit. Table A2 records the corrections. Such trajectories cannot establish hardware DC safety or physical recovery.

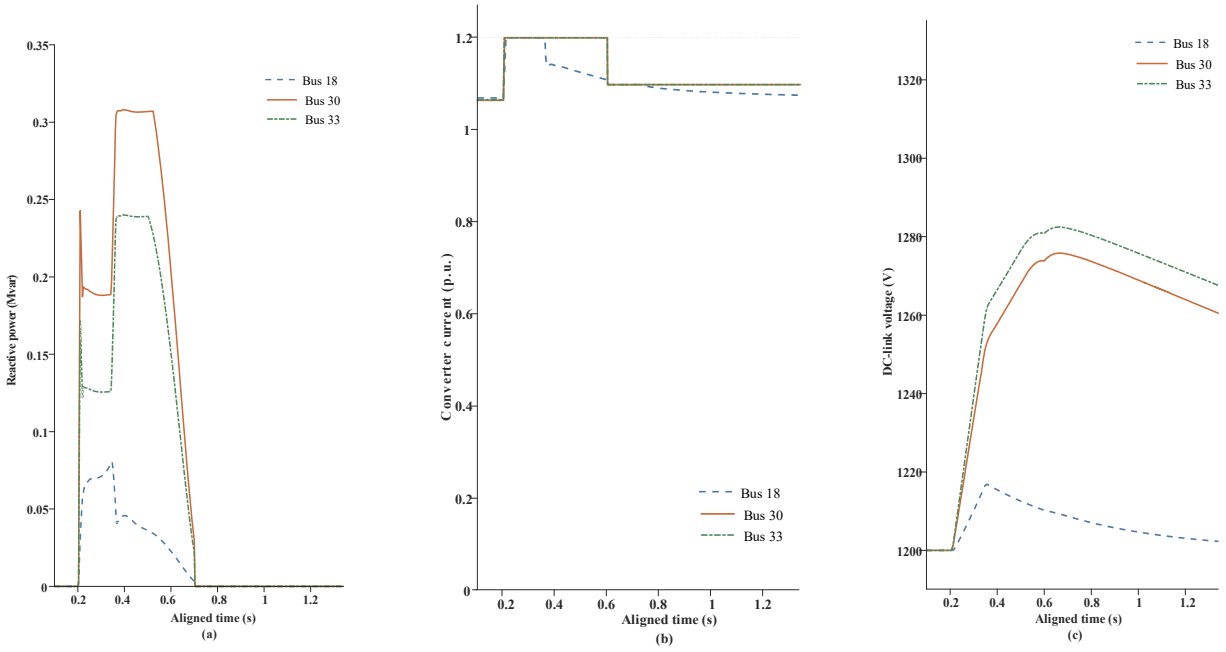


Figure 11. Site-level DPV trajectories under Full CTVS for the 140 ms fault: (**a**) reactive-power outputs; (**b**) converter current magnitudes; and (**c**) DC-link voltages.

5.4. Spatial Sensitivity Validation

H20 applies a 20 kvar bias per site with supplementary CTVS feedback disabled. Symmetric ±5/±10 kvar pulses begin at 4.0 s and are evaluated at 40 ms without current saturation. The Q request is converted through filtered site voltage and rating to a current target, whereas realized Q depends on interface voltage and limited current. Motor, filter, and DC states evolve; Appendix B records the pulse duration and pre-state. Figure 12 compares the normalized finite-horizon sensitivities and prescribed spatial weights under H20, together with the short-horizon Bus-30 voltage responses under the current-saturated F140 condition.

The corresponding finite-horizon dynamic sensitivities under H20 and F140 are summarized in Table 3.

Table 4 uses the saved pre-4.0 s H20 source, feeder, RLC-load and transformer parameters, with motor terminal P/Q frozen to isolate the network–converter algebraic mapping from the evolving SPS motor response evaluated in Table 3. Its 70 × 70 phasor Jacobian approximates the sampled interface quasi-statically: the held voltage is identified with the nodal voltage. $\mathbf{K}_{PV}$ then has PV entries −0.0218171/−0.0217289/−0.0217442 p.u. Q per p.u. V, counted once; these are not the dynamic gains 4/9/0.008. The actual interface uses 50 μs voltage memories. A separate held-memory calculation has zero direct current-voltage feedback, preserves the site ordering, and agrees with twelve nonlinear perturbations within 0.070% (Table A3). Neither calculation validates the complete SPS electrical-state DAE.

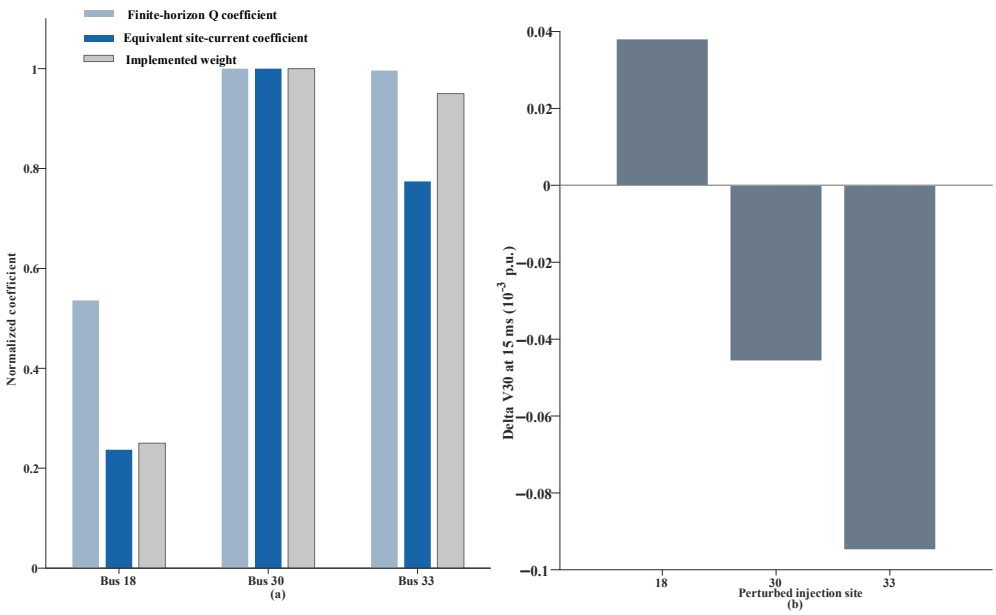


Figure 12. Spatial voltage-support sensitivity validation: (**a**) normalized 40 ms finite-horizon gains versus prescribed weights under pre-fault condition H20 and (**b**) 15 ms Bus-30 voltage increments under current-saturated fault condition F140.

Table 3. Finite-Horizon Dynamic Sensitivities Across DPV Sites under H20 and F140 Conditions. (n/a denotes not applicable. For the current-limited F140 condition, the mixed-sign finite-horizon G_Q values are not normalized using the positive-gain criterion adopted for H20. The equivalent site-current gains $G_{i,eq}$ are not reported because the unsaturated Q-to-current-command conversion is not applicable under active current limits.

Operating Condition	Bus	ΔQ_{cmd} (kvar)	ΔQ_{real} (kvar)	G_Q (p.u./Mvar)	Norm. G_Q	$G_{i,eq}$ (p.u./p.u.)/Norm.	Prescribed w_j
H20, 40 ms	18	+/−5; +/−10	10.000; 20.000	0.017023	0.5356	0.003121/0.2371	0.25
H20, 40 ms	30	+/−5; +/−10	10.000; 20.000	0.031781	1.0000	0.013163/1.0000	1.00
H20, 40 ms	33	+/−5; +/−10	10.000; 20.000	0.031652	0.9960	0.010190/0.7741	0.95
F140, 15 ms	18	+/−5	10.015	0.003791	n/a	n/a	0.25
F140, 15 ms	30	+/−5	4.980	−0.009151	n/a	n/a	1.00
F140, 15 ms	33	+/−5	4.801	−0.019721	n/a	n/a	0.95

Table 4. Quasi-Static Frozen-P/Q Algebraic Sensitivities Across DPV Sites (H20).

Bus	$\eta_{30,j}^{cmd}$ (p.u./Mvar)	Norm. $\eta_{30,j}^{cmd}$	$g_{i,j}$ (p.u./p.u.)	Norm. $g_{i,j}$	Prescribed w_j	Max. Error (%)
18	0.01744648	0.5360	0.00319868	0.2373	0.25	0.031942
30	0.03254895	1.0000	0.01348159	1.0000	1.00	0.009754
33	0.03239892	0.9954	0.01043003	0.7736	0.95	0.016022

Equivalent Q commands enter the post-slew interface through $\Delta i_{q,j} = \frac{\Delta Q_{c,j}}{S_j V_{f,j,0}}$; realized Q additionally depends on voltage. Twelve ±1/±5 kvar nonlinear algebraic solves retain the inactive-limit set and agree with predictions within 0.031942%. This validates the reconstructed frozen-P/Q approximation, not the complete SPS–DAE.

At H20, paired realized-Q changes match the 10/20 kvar command differences within 0.05 var. The converted current coefficient in Table 3 is not an independently identified current-input derivative. A 1 MVA system base makes 1 Mvar equal 1 p.u. Q, but site-current bases differ.

F140 applies ±5 kvar at 4.05 s for 20 ms, evaluated at 15 ms with all sites at 1.20 p.u. The mixed-sign coefficients in Table 3 include current-circle coupling, active-power displacement, slew limits, and evolving states; they are not static network derivatives.

Under unsaturated condition H20, both the finite-horizon dynamic gains and the frozen-P/Q algebraic sensitivities confirm the spatial effectiveness ordering Bus 30 > Bus 33 > Bus 18, consistent with the prescribed participation ordering. The normalized site-current sensitivity vector is 0.2373/1.0000/0.7736 and does not reproduce the prescribed numerical weights exactly. Conversely, F140 demonstrates that at the 1.20-p.u. current-limited operating point, active-power displacement and current-circle coupling alter the local incremental gains, so the unsaturated positive-support ordering does not transfer to a saturated active set.

At the unsaturated quasi-static H20 point of Table 4, the first-order critical-voltage response ratios $\Delta V30/\Delta Q$ are 0.02418979, 0.02256933, and 0.02230931 p.u. for the Original prescribed coefficients (0.25/1.00/0.95), Uniform coefficients (0.8325), and auxiliary current-sensitivity coefficients (0.2373/1.0000/0.7736), respectively. Normalizing by the nominal fixed-voltage fleet reactive-power increments yields effective support gains Geff of 0.03158052, 0.02948090, and 0.03156165 p.u./Mvar (Table A4). Thus, at this linearized unsaturated point, the prescribed coefficients yield a 7.12% higher gain per unit nominal reactive-power increment than Uniform allocation, while their scalar effective gain differs by less than 0.06% from that of the auxiliary sensitivity-based allocation. This compares local gains, not vector distance or global optimality.

Independent auxiliary time-domain simulations retaining all physical parameters, gains, initialization, and current-limit timing were conducted using the unscaled sensitivity vector (0.2373/1.0000/0.7736, capacity-weighted request 0.76822) and its budget-matched scaled vector (multiplied by 1.083674 to match the 0.8325 nominal budget of Original and Uniform). Both auxiliary configurations and the Original/Uniform controllers pass at the 140 ms and 147 ms opening commands and fail at 148 ms, with 140 ms sustained voltage-recovery delays of 23.85, 23.85, 23.85, and 23.80 ms, respectively. Together with Table A4, these results distinguish a local unsaturated allocation-gain advantage from large-disturbance recovery: common converter limits constrain fault-on operation, while the matched ablations identify slip-conditioned persistence as the primary recovery contribution. Current saturation does not establish identical site-level reactive injection or an optimal weight vector.

5.5. Robustness and Model Limitations

The final study varies IM inertia and external constant load torque separately around J_0 = 6 kg·m² and $T_{load,0}$ = 1850 N m. The ratios are J/J_0 = 0.8, 1.0, 1.2 and $T_{load}/T_{load,0}$ = 0.9, 1.0, 1.1. Viscous friction remains fixed; these load ratios do not vary the total opposing torque including friction in Equation (9). Each case is reinitialized and checked for a stable pre-fault state. The network, 140 ms fault, controller gains, converter constraints, and DC implementation remain fixed, without cross-combinations. The corresponding Bus-30 voltage and IM slip responses under the IM parameter variations are shown in Figure 13.

https://doi.org/10.3390/sym18111859

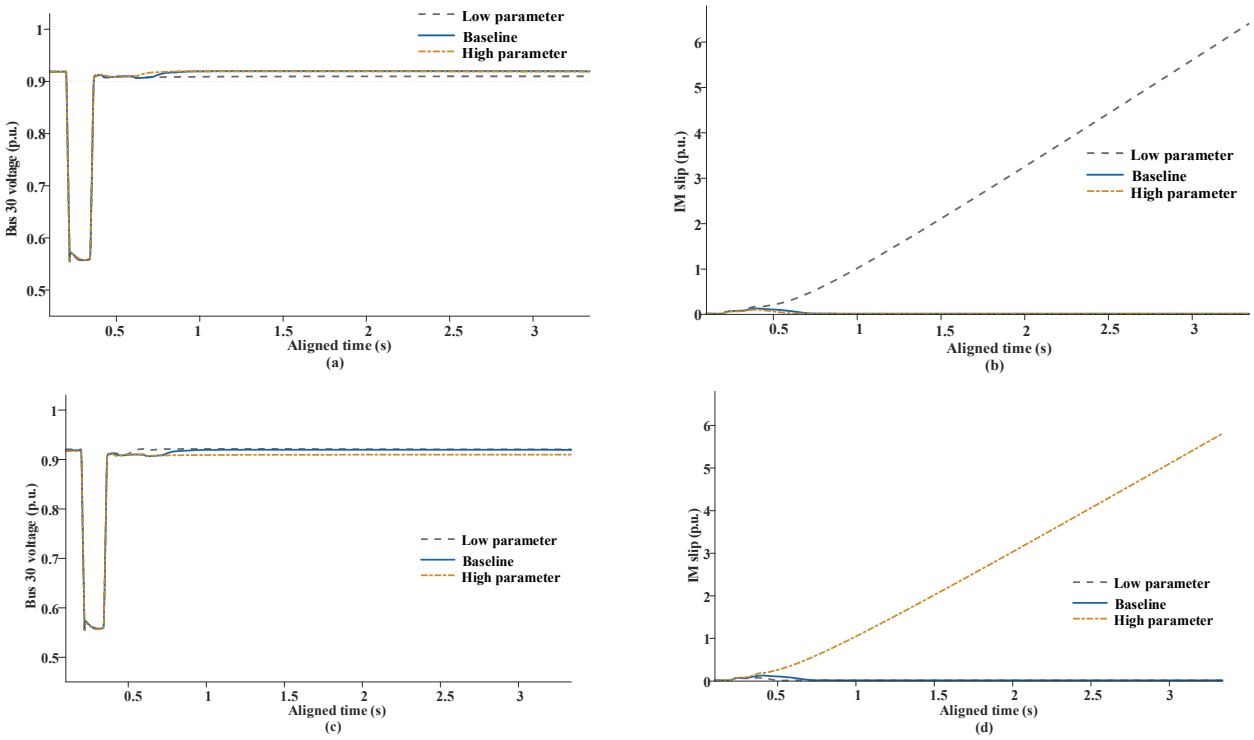


Figure 13. Sensitivity of Full CTVS to IM parameter variations under the 140 ms fault: (**a**,**b**) Bus-30 voltage and IM slip for J/J_0 = 0.8, 1.0, 1.2; (**c**,**d**) Bus-30 voltage and IM slip for $T_{load}/T_{load,0}$ = 0.9, 1.0, 1.1.

The three controllers have identical classifications in Table 5: baseline, higher inertia, and lighter external load pass; lower inertia and heavier load fail. CTVS can satisfy the voltage interval in about 24 ms while the motor fails. These one-at-a-time cases identify operating-point sensitivity, not an enlarged inertia/load recovery region.

Table 5. Joint Recovery Classification Under Single-Factor IM Parameter Variations (140 ms Fault).

Parameter Type	Variation Ratio	Corrected Local LVRT	Adaptive Q–V Droop	Full CTVS
Inertia	J/J_0 = 0.8	Fail	Fail	Fail
Inertia	J/J_0 = 1.0	Pass	Pass	Pass
Inertia	J/J_0 = 1.2	Pass	Pass	Pass
Mechanical torque	$T_{load}/T_{load,0}$ = 0.9	Pass	Pass	Pass
Mechanical torque	$T_{load}/T_{load,0}$ = 1.0	Pass	Pass	Pass
Mechanical torque	$T_{load}/T_{load,0}$ = 1.1	Fail	Fail	Fail

The machine omits saturation and thermal, contactor, mechanical-stop, and protection models. Slip above 1 is numerical extrapolation, not a validated reversal prediction. In the adverse CTVS cases, slip crosses 0.5 before both s = 1 and the later DC clamp, so model failure is established before those extrapolations; subsequent trajectories cannot quantify physical motor or converter behavior.

For $k_v = 4$, $k_s = 9$, and $k_r = 0.008$, illustrative inputs of a 0.05-p.u. normalized voltage deficit, a 0.02 excess slip, and a 1-p.u./s voltage-decrease rate contribute 0.20, 0.18, and 0.008 to the common support signal before site weighting and limiting. These values show the intended relative scales of voltage, slip, and voltage-rate feedback.

Four one-factor runs change k_v to 3.6/4.4 or k_s to 8.1/9.9 under the same 140 ms fault, while retaining k_r, the spatial coefficients, initialization, and all converter constraints. Together with the nominal baseline, all five cases jointly recover with the same sampled sustained delay of 23.85 ms. Their peak DC-link voltages range from 1278.49 to 1285.02 V without numerical clipping (Table A6). The Bus-30 and Bus-33 requests reach the 0.75 p.u. target cap, and their currents reach the 1.20-p.u. limit during the fault and initial rebound, helping explain the unchanged sampled sustained-recovery delay despite modest differences in the DC-link transient.

6. Conclusions

This study presented a coordinated transient voltage support strategy combining induction motor slip feedback with multi-site distributed photovoltaic reactive-current regulation. The coupled DAE model and trajectory-local closed-loop Q–V sensitivity analysis characterize location-dependent support effectiveness across candidate feeder buses. At the unsaturated H20 operating point, the fixed spatial participation coefficients achieve a 7.12% higher local voltage-support gain per unit nominal reactive-power increment than uniform allocation, although this allocation benefit remains confined to the unsaturated regime.

Under the matched 140 ms Bus-32 fault, CTVS suppresses secondary voltage depression and reduces the sustained recovery delay to 23.85 ms versus 342.30 ms for local LVRT and 390.85 ms for adaptive Q–V droop, trading greater transient active-power curtailment and a 1282.45 V DC-link peak for accelerated voltage restoration. Matched ablations confirm that slip-conditioned support persistence is the primary contributor to large-disturbance recovery, as uniform and prescribed weights recover almost identically and share the 147 ms-pass/148 ms-fail opening-command bracket. Shorter-fault, criterion-sensitivity, local gain, and motor-parameter tests further delimit these findings: the timing advantage is threshold-dependent, the command bracket is not an exact physical CCT, and the tested motor-parameter classifications remain identical across controllers. Validation is restricted to the modified IEEE 33-bus feeder and tested Bus-32 three-phase faults, while online weight adaptation, unbalanced faults, and hardware DC protection are left for future work.

Author Contributions: Conceptualization, T.Z. and W.X.; methodology, T.Z.; software, T.Z. and C.W.; validation, Y.Z. and Y.W.; formal analysis, T.Z. and W.X.; investigation, Y.Z.; resources, W.X.; data curation, C.W. and Y.W.; writing—original draft preparation, T.Z.; writing—review and editing, W.X., Y.Z. and Y.W.; visualization, T.Z. and C.W.; supervision, T.Z.; project administration, T.Z.; funding acquisition, T.Z. All authors have read and agreed to the published version of the manuscript.

Funding: This work was supported by the Natural Science Foundation of Jiangsu Province (No. BK20241481) and the Medium-to-Long-Term Overseas Training Special Program for Key Young Scientific Talents of the Ministry of Industry and Information Technology (MIIT) of China (No. T241012003).

Data Availability Statement: Reproduction data and verification results are provided in the article and Appendices A–C. Native Simulink models and time-series archives are available from the corresponding author upon request.

Conflicts of Interest: The authors declare no conflicts of interest.

Appendix A. Essential Implementation and DC-Energy Checks

Table 1 specifies the common plant, controller, current-limit, and DC-link settings, while Table A1 provides the additional electrical and initialization details required for reproduction. The implemented feeder retains the IEEE 33-bus topology at 12.66 kV. Its extracted nominal static bus loads total 3745 kW and 2310 kvar before the additional 20 kW Load34 block at Bus 33 and three 1 W DPV interface shunts; including these additions gives 3765.003 kW and 2310 kvar, excluding the separately modeled IM. The 315 kVA SPS induction motor and 500 kVA transformer are connected at Bus 30, and the averaged DPV units are connected at Buses 18, 30, and 33. Static loads are implemented as 50 Hz parallel RLC impedance branches rather than ideal constant-power sinks. The implemented branch impedances and load ratings are taken from the saved modified model; the complete extracted branch and nominal bus-load records are listed in Table A5, with initialization and numerical settings in Appendix C.

Table A1. Additional implemented parameters.

Item	Implemented Value	Basis/Interpretation
Source impedance	R = 0.228965 Ω; X = 1.602756 Ω; L = 0.00510173 H	Active 100 MVA short-circuit/X/R = 7 setting
IM equivalent circuit	R_s/R_r = 0.0076/0.0061 Ω; L_{ls}/L_{lr} = 1.62 × 10^{-4} H; L_m = 4.85 × 10^{-3} H	Single-cage, 315 kVA, 400 V base; magnetic saturation disabled
IM startup	Slip 0.0186699; angle 0°; phase currents 812.169 A at −3.12819°, −123.128°, 116.872°	Saved Simulink block initial phasor magnitudes/angles prior to warm-up; re-equilibrated during the common 4 s warm-up to the pre-fault operating state
Transformer	500 kVA, D1/Yg; per-winding R/X = 0.005/0.04 p.u.; $R_m = L_m$ = 500 p.u.	12.66/0.4 kV; nonsaturating core
Additional loads	Load34: 20 kW, 0 kvar, 12 kV nominal, physically at Bus 33; three DPV shunts: 1 W each	Complete nominal feeder records in Table A5; additions retain their own nominal-voltage bases

The same saved machine state and controller initialization are used for the matched comparisons. Fault inception is at physical 4.0 s after warm-up; the common 140 ms pre-fault means are 0.918778 p.u. at Bus 30 and slip 0.017164. The opening command, 100 ms hold, 1 s TVSI and command-plus-3 s joint-screen definitions remain those in Section 5.1.

Table A2. Full CTVS DC-energy audit at the 140- and 160 ms opening commands.

DPV Bus	140 ms ΔEcap (kJ)	140 ms $\int(P_{dc} - P_{ac})\,dt$ (kJ)	Euler Correction (J)	160 ms Clamp Correction (kJ)
18	0.0076	0.0076	0.0116	−20.49
30	5.2911	5.2908	0.2570	−103.01
33	7.6957	7.6955	0.2553	−83.37

The audit uses 50 μs updates on [t_{on}, t_{cmd} + 3 s), with pre-update capacitor states at its endpoints. P_{dc} is the imposed DC input and Pac is enforced average-interface power, not an independent hardware measurement. Including the explicit Euler energy correction gives residuals below 1.3 × 10^{-8} J in the unclamped 140 ms case (maximum DC voltage

1282.45 V). At 160 ms, the negative clamp corrections have no modeled physical dissipation path. The 1320 V level is assessment only; 1600 V is a numerical clamp, not protection.

Appendix B. Essential Spatial Sensitivity and Weight Checks

H20 uses a 20 kvar bias per DPV from 3.5 s, with supplementary CTVS feedback disabled. The saved pre-pulse point is at 3.99995 s: logged Bus 18/30/33 voltages are 0.916713/0.920432/0.919786 p.u., slip is 0.017084, and motor-terminal consumption is 298.0353216 kW/157.6540202 kvar. The system base is 1 MVA; site current bases use 0.20/0.45/0.35 MVA. Floor, current-circle, target-cap and residual active-power limits are inactive at this point.

Table A3. Quasi-static interface conditions and distinct held-memory cross-check.

Bus	$V_{f,0}$ (p.u.)	$V_{0,qs}$ (p.u.)	$i_{q,0}$ (Site p.u.)	$K_{PV,qs}$ (p.u.Q/p.u.V)	$\eta_{cmd,held}$ (p.u./Mvar)	$g_{i,held}$ (p.u./Site p.u.)	Held Max. Error (%)
18	0.91671322	0.91679269	0.10908537	−0.02181707	0.01739405	0.00318907	0.069739
30	0.92043189	0.92059254	0.04828651	−0.02172893	0.03249086	0.01345753	0.027347
33	0.91978614	0.91989604	0.06212624	−0.02174419	0.03233408	0.01040915	0.040153

$V_{0,qs}$ is the reconstructed quasi-static voltage (maximum deviation from the logs 1.61 × 10^{-4} p.u.). Its K_{PV} entries represent the $Q_j = S_j V_j i_{q,j}^{sup}$ interface dependence counted once, rather than the controller gains 4/9/0.008. The quasi-static command coefficient is $B_{u,Q,j} = \frac{V_{0,qs,j}}{V_{f,0,j}}$. Freezing the actual 50 μs voltage memory instead gives K_{PV} = 0 with respect to current network V, with held voltages 0.91671320/0.92043183/0.91978608 p.u. Frozen filters add no instantaneous control gain. Equivalent Q commands enter after slew conversion; the corresponding current sensitivity is $g_{i,j} = \eta_{30,j}^{cmd} S_j V_{f,0,j}$. Neither phasor approximation restores the complete SPS electrical-state DAE.

The twelve ±1/±5 kvar nonlinear algebraic checks remain within the inactive-limit set (maximum current 1.0773 p.u. < 1.10). Table 4 retains the distinct quasi-static maximum error of 0.031942%; the held-memory check has maximum error below 0.070% and residual below 1.3 × 10^{-12} p.u. Signed predictions, errors and residuals are retained by the authors and are available upon reasonable request.

The evolving-state tests differ: H20 ±5/±10 kvar pulses start at 4.0 s for 50 ms and are evaluated at 40 ms. F140 ±5 kvar pulses start at 4.05 s for 20 ms and are evaluated at 15 ms, with all sites at 1.20 p.u. Their paired realized-Q differences are 10.015/4.980/4.801 kvar; the mixed-sign coefficients in Table 3 include saturation, active-power displacement and state evolution, not static network derivatives.

Table A4. A posteriori local allocation comparison at the quasi-static H20 point.

Scheme	w18/w30/w33	$\Sigma S_j w_j$	ΔV30/ΔQ	Nominal ΔQ/ΔQ Mvar	Geff p.u./Mvar
Original	0.2500/1.0000/0.9500	0.83250	0.02418979	0.76597171	0.03158052
Uniform	0.8325/0.8325/0.8325	0.83250	0.02256933	0.76555767	0.02948090
Auxiliary raw	0.2373/1.0000/0.7736	0.76822	0.02230931	0.70684868	0.03156165

Auxiliary matched	0.2572/1.0837/0.8383	0.83250	0.02417602	0.76599350	0.03156165

The voltage coefficient is $\sum g_i w_j$; the denominator of Geff is the nominal coefficient $\sum_j S_j V_{0,\mathrm{qs},j} w_j$ at frozen voltages, not the nonlinear realized-Q derivative. These are independent post-slew allocation directions with gate/limiter transitions excluded. Original is 7.12% above Uniform in this local ratio and within 0.06% of the unscaled auxiliary direction; this does not derive the prescribed weights or prove optimality. The auxiliary matched vector scales the raw vector by 1.0836739476 to match the nominal budget, not the realized Q.

Appendix C. Reproduction Data and Additional Checks

Table A5 gives the actual radial branches and principal static bus loads of the modified saved model. The balanced source is at Bus 1, 12.66 kV line-to-line, 50 Hz, angle 0°. Branch inductance is listed directly; reactance is X = 2π50 L. All principal loads use 12.66 kV nominal voltage and constant-impedance RLC dynamics at 50 Hz. Their nominal totals are 3745 kW and 2310 kvar. The separately listed additions in Table A1 are a 20 kW, 12 kV nominal load at Bus 33 and one 1 W shunt at each DPV site; the IM and transformer are separate devices. The saved E1 and E2 physical-model files match the archived parameter-audit hashes, with 109 physical blocks previously compared as identical.

Table A5. Implemented feeder branches and principal nominal bus loads.

Branch	R (Ω)	L (mH)	Load Bus	P (kW)	Q (kvar)
1–2	0.0922	0.129552	2	100	60
2–3	0.4930	0.799276	3	90	40
3–4	0.3660	0.593330	4	120	80
4–5	0.3811	0.617839	5	60	30
5–6	0.8190	2.250451	6	60	20
6–7	0.1872	1.969702	7	200	100
7–8	0.7144	1.496693	8	200	100
8–9	1.0300	2.355493	9	60	20
9–10	1.0440	2.355493	10	60	20
10–11	0.1966	0.206901	11	45	30
11–12	0.3744	0.394068	12	60	35
12–13	1.4680	3.676479	13	60	35
13–14	0.5416	2.269231	14	120	80
14–15	0.5910	1.674310	15	60	10
15–16	0.7463	1.734789	16	60	20
16–17	1.2890	5.478113	17	60	20
17–18	0.7320	1.827099	18	120	50
2–19	0.1640	0.498155	19	90	40
19–20	1.5042	4.314372	20	90	40

20–21	0.4095	1.522794	21	90	40
21–22	0.7089	2.983519	22	90	40
3–23	0.4512	0.981349	23	90	50
23–24	0.8980	2.257135	24	420	200
24–25	0.8960	2.231671	25	420	200
6–26	0.2030	0.329132	26	60	25
26–27	0.2842	0.460594	27	60	25
27–28	1.0590	2.972059	28	60	20
28–29	0.8042	2.230079	29	120	70
29–30	0.5075	0.822831	30	200	600
30–31	0.9744	3.065324	31	150	70
31–32	0.3105	1.151963	32	210	100
32–33	0.3410	1.687679	33	60	40

The MATLAB/Simulink-R2024b model uses a 50 μs discrete electrical step, powergui Backward Euler, and fixed-step ode3. All matched cases start from the saved IM conditions in Table A1 and run a 4 s warm-up; the fault is inactive and supplementary reactive support is zero before t = 4 s. The source short-circuit setting and source impedance are given in Tables 1 and A1. Fault switches connect all three phases at Bus 32 with 8 Ω branch resistance and 0.01 Ω ground resistance; the opening command is 4 s plus the specified duration. Phase-current extinction times are not separately logged.

Controller initialization is $v_r = [0.93, 0.96, 0.95]$ p.u., critical filtered voltage 0.924 p.u., previous normalized critical voltage 1, i_q command zero, and $U_{dc} = [1200, 1200, 1200]$ V. The available-power vector is [196, 441, 343] kW. Site and critical filters use $a = \exp(-T_s / \tau)$ with $\tau = 2$ and 4 ms. Slip feedback is $\max[0, 1 - \omega_m / (2\pi 50/2)]$. The healthy-voltage reference for Droop is the mean filtered site voltage over [3.8, 4.0) s, and its active-power estimator starts at the available-power vector and updates causally with $T_s / 0.020$. The common terminal-voltage memory is one sample (50 μs); the averaged-interface voltage floor is 0.05 p.u. The external-P/Q-load interface receives $[-P, -Q]$ to represent generation and uses zero P/Q exponents and command time constants, with its internal voltage filter set to 0.1 ms. Reproduction requires these dynamics as well as the network ratings.

The common DC-link voltage is updated using explicit Euler discretization of Equation (5): $U_{\mathrm{dc,next}} = \mathrm{clip}\left(U_{\mathrm{dc}} + \dfrac{T_s (P_{\mathrm{dc}} - P_{\mathrm{ac}})}{\max(C_{\mathrm{dc}}, 0.05\ \mathrm{F}) \max(U_{\mathrm{dc}}, 800\ \mathrm{V})}, 900\ \mathrm{V}, 1600\ \mathrm{V} \right)$.

The implemented DC-link capacitances are 0.20, 0.45, and 0.35 F, respectively, all exceeding the 0.05-F numerical lower bound. P_{ac} denotes the nonnegative active-power transfer limited by the available current headroom. The DC-voltage feedback gains are 500, 1125, and 875 W/V, respectively, with a reference voltage of 1200 V. The 1320 V level is used only as an assessment threshold. Numerical clipping does not represent physical energy dissipation or hardware protection; its energy effect is quantified in Appendix A. The same DC-link implementation is retained in the nominal and gain-sensitivity cases. Equations (14) and (15) were checked by central differences with steps 10^{-4}, 10^{-5}, and 10^{-6} at three specified algebraic states, giving a maximum absolute discrepancy of 1.47 ×

10^{-9}. This checks the algebraic derivatives, not a recovered SPS electromagnetic trajectory or complete SPS-DAE Jacobian.

For reproduction of the algebraic differentiation check, $R_s = 0.0149625$ p.u. and $X' = 0.1971557257$ p.u. are obtained from the Table-A1 circuit on the 315 kVA, 400 V base. The three test vectors $(V, \theta, E'_d, E'_q, s)$, with θ in radians, are (0.92, 0.10, 0.87, −0.03, 0.017), (0.65, −0.20, 0.70, 0.08, 0.13), and (1.00, 0.30, 0.96, 0.12, 0.02). Each central difference varies one scalar while freezing the other four.

Table A6. Local gain sensitivity for the 140 ms fault with all other settings fixed.

Setting	k_v	k_s	Sustained (ms)	$TVSI_{1s}$ (p.u.·s)	Peak Slip	Peak U_{dc} (V)	Joint
Nominal	4	9	23.85	0.004511	0.131213	1282.45	Pass
k_v − 10%	3.6	9	23.85	0.004512	0.131212	1282.42	Pass
k_v + 10%	4.4	9	23.85	0.004510	0.131215	1282.48	Pass
k_s − 10%	4	8.1	23.85	0.004512	0.131223	1278.49	Pass
k_s + 10%	4	9.9	23.85	0.004511	0.131203	1285.02	Pass

Table A6 uses the recovery and TVSI definitions in Section 5.1. The nominal row is retained; the other four rows are new one-factor runs with all remaining settings unchanged. Raw trajectories, initialization comparisons, and run configurations are retained by the authors. The 19 pre-fault channels match within 10^{-12}.

References

1. Hatziargyriou, N.; Milanović, J.V.; Rahmann, C.; Ajjarapu, V.; Cañizares, C.; Erlich, I.; Hill, D.; Hiskens, I.; Kamwa, I.; Pal, B.; et al. Definition and classification of power system stability—Revisited and extended. *IEEE Trans. Power Syst.* **2021**, *36*, 3271–3281.
2. Ali, J.S.; Qiblawey, Y.; Alassi, A.; Massoud, A.M.; Muyeen, S.M.; Abu-Rub, H. Power system stability with high penetration of renewable energy sources: Challenges, assessment, and mitigation strategies. *IEEE Access* **2025**, *13*, 39912–39934.
3. *IEEE Std 1547a-2020*; IEEE Standard for Interconnection and Interoperability of Distributed Energy Resources with Associated Electric Power Systems Interfaces—Amendment 1. IEEE: New York, NY, USA, 2020.
4. Alrumayh, O.; Sayed, K.; Almutairi, A. LVRT and reactive power/voltage support of utility-scale PV power plants during disturbance conditions. *Energies* **2023**, *16*, 3245.
5. Yan, X.; Liang, B.; Jia, J.; Aslam, W.; Wang, C.; Zhang, S.; Ma, H. Strategies to increase the transient active power of photovoltaic units during low voltage ride through. *Energies* **2021**, *14*, 5236.
6. Zhou, T.; Zheng, Y.; Wang, C.; Chen, L.; Liu, B.; Chen, Z. Small-signal modeling and frequency support capacity analysis of power load considering voltage variation effect. *Symmetry* **2024**, *16*, 918.
7. Chen, L.; Wang, X.; Min, Y.; Li, G.; Wang, L.; Qi, J.; Xu, F. Modelling and investigating the impact of asynchronous inertia of induction motor on power system frequency response. *Int. J. Electr. Power Energy Syst.* **2020**, *117*, 105708.
8. Bu, F.; Ma, Z.; Yuan, Y.; Wang, Z. WECC composite load model parameter identification using evolutionary deep reinforcement learning. *IEEE Trans. Smart Grid* **2020**, *11*, 5407–5417.
9. Lammert, G.; Premm, D.; Pabón Ospina, L.D.; Boemer, J.C.; Braun, M.; Van Cutsem, T. Control of photovoltaic systems for enhanced short-term voltage stability and recovery. *IEEE Trans. Energy Convers.* **2019**, *34*, 243–254.
10. Wang, W.; de León, F. Quantitative evaluation of DER smart inverters for the mitigation of FIDVR in distribution systems. *IEEE Trans. Power Deliv.* **2020**, *35*, 420–429.
11. Varma, R.K.; Mohan, S. Mitigation of fault induced delayed voltage recovery (FIDVR) by PV-STATCOM. *IEEE Trans. Power Syst.* **2020**, *35*, 4251–4262.
12. Wang, S.; Du, L.; Fan, X.; Huang, Q. Deep reinforcement scheduling of energy storage systems for real-time voltage regulation in unbalanced LV networks with high PV penetration. *IEEE Trans. Sustain. Energy* **2021**, *12*, 2342–2352.

13. Hu, Y.; Liu, W.; Wang, W. A two-layer Volt-Var control method in rural distribution networks considering utilization of photovoltaic power. *IEEE Access* **2020**, *8*, 118417–118425.
14. Gao, X.; Zhang, J.; Sun, H.; Liang, Y.; Wei, L.; Yan, C.; Xie, Y. A review of voltage control studies on low voltage distribution networks containing high penetration distributed photovoltaics. *Energies* **2024**, *17*, 3058. https://doi.org/10.3390/en17133058.
15. Ilea, V.; Bovo, C.; Falabretti, D.; Merlo, M.; Arrigoni, C.; Bonera, R.; Rodolfi, M. Voltage control methodologies in active distribution networks. *Energies* **2020**, *13*, 3293.
16. Maataoui, Y.; Chekenbah, H.; Boutfarjoute, O.; Puig, V.; Lasri, R. A coordinated voltage regulation algorithm of a power distribution grid with multiple photovoltaic distributed generators based on active power curtailment and on-line tap changer. *Energies* **2023**, *16*, 5279.
17. Hassan, A.S.J.; Marikkar, U.; Prabhath, G.W.K.; Balachandran, A.; Bandara, W.G.C.; Ekanayake, P.B.; Godaliyadda, R.I.; Ekanayake, J.B. A sensitivity matrix approach using two-stage optimization for voltage regulation of LV networks with high PV penetration. *Energies* **2021**, *14*, 6596.
18. Azarnia, M.; Rahimiyan, M. Robust Volt-Var control of a smart distribution system under uncertain voltage-dependent load and renewable production. *Int. J. Electr. Power Energy Syst.* **2022**, *134*, 107383.
19. Guo, Y.; Wu, Q.; Gao, H.; Chen, X.; Østergaard, J.; Xin, H. MPC-based coordinated voltage regulation for distribution networks with distributed generation and energy storage system. *IEEE Trans. Sustain. Energy* **2019**, *10*, 1731–1739.
20. Jabr, R.A. Robust Volt/VAr control with photovoltaics. *IEEE Trans. Power Syst.* **2019**, *34*, 2401–2408.
21. Lv, Z.; Wang, B.; Guo, Q.; Sun, H. Optimal grid-support strategy with inverter-interfaced distributed generators for short-term voltage stability improvement. *IEEE Trans. Sustain. Energy* **2024**, *15*, 499–512.
22. Owais, R.; Javed Iqbal, S. Utility-scale solar photovoltaic power plant emulating a virtual synchronous generator with simultaneous frequency and voltage control provision. *IET Energy Syst. Integr.* **2024**, *6*, 386–405.

Disclaimer/Publisher's Note: The statements, opinions and data contained in all publications are solely those of the individual author(s) and contributor(s) and not of MDPI and/or the editor(s). MDPI and/or the editor(s) disclaim responsibility for any injury to people or property resulting from any ideas, methods, instructions or products referred to in the content.